

## From the Lebombo Monocline to the Mozambique Deep Basin, using combined wide-angle and reflection seismic data

Moulin Maryline <sup>1,\*</sup>, Leprêtre A. <sup>1</sup>, Verrier Fanny <sup>1</sup>, Schnürle Philippe <sup>1</sup>, Evain Mikael <sup>1</sup>, De Clarens P. <sup>2</sup>, Thompson Joseph Offei <sup>1,3</sup>, Dias N. <sup>4</sup>, Afilhado A. <sup>5</sup>, Loureiro A. <sup>4</sup>, Aslanian Daniel <sup>1</sup>

<sup>1</sup> Geo-Ocean, Univ Brest, CNRS, Ifremer, UMR6538, F-29280 Plouzane, France

<sup>2</sup> TOTAL, R&D, avenue Larribau, 64000 Pau, France

<sup>3</sup> Univ. of Ghana, Department of Geology, Accra, Ghana

<sup>4</sup> IDL – Instituto Dom Luis, Faculdade das Ciencias da Universidade de Lisboa, 1749-016 Lisboa, Portugal

<sup>5</sup> ISEL – Instituto Superior de Engenharia de Lisboa, Lisboa, Portugal

\* Corresponding author : Maryline Moulin, email address : [mmoulin@ifremer.fr](mailto:mmoulin@ifremer.fr)

### Abstract :

The North Natal valley (NNV), South Mozambique margin, is a key area for the understanding of the SW Indian Ocean history since the Gondwana break-up as its crustal nature and geometry strongly impacted the reconstruction of the paleogeography before the rifting. It is also of considerable importance for the understanding of the evolution of a margin system as the NNV is situated at the transition between divergent and strike-slip segments and at the conjunction of Oxfordian-Kimmeridgian Indian Ocean and the Valanginian-Aptian Atlantic one. As one part of the PAMELA project (PASSive Margins Exploration Laboratories), the NNV and the East Limpopo margin have been investigated during the MOZ3/5 cruise (2016), through the acquisition of 7 intersecting wide-angle profiles and coincident marine multichannel (720 traces) seismic as well as potential field data. Simultaneously, land seismometers were deployed in the Mozambique coastal plain (MCP), extending six of those profiles on land for about 100 km in order to provide information on the onshore-offshore transition. Wide-angle seismic data are of major importance as they can highlight constraints on the crustal structure of the margin and the position of the continent-ocean boundary in an area where the crustal nature is poorly known and largely controversial. The MOZ3/5 data set therefore reveals new essential constraints for kinematic reconstructions. This work presents results on the crustal structure from P-waves velocity modeling along two E-W wide-angle profiles (MZ1 and MZ2) through the NNV, from the Lebombo Monocline to the Mozambique Basin (MB), and crossing the Mozambique Fracture Zone (MFZ).

The new geophysical data reveals an upper sedimentary sequence characterized by low velocities generally not exceeding 3 km/s, and up to 3 km thick where a major contouritic structure was observed. This feature forms together with several other contouritic structures, a N-S alignment just west of the MFZ, which produces high positive gravity anomalies, previously thought to be related to the magmatism that built the Galathea and Dana Plateaus. High velocity lenses are locally identified through the sedimentary layers and interpreted as inter-bedded volcanic sills. Furthermore, from the NNV to the MFZ, the underlying sequence is formed of a 3.0–3.5 km thick volcano-sedimentary sequence presenting

---

important lateral changes in its seismic signature and characterized by a large velocity range (4.4 to 5.8 km/s), which partly reflects variations in the volcanic/sedimentary ratio laterally and with depth. At depth, an initially smoother and reduced eastward thinning of the crust occurs to the West below the continental shelf, from 34 to 31 km thick. The crustal thickness remains relatively constant of about 28–29 km along the Central Domain (CD), whereas a second and major region of thinning (26 to 12 km thick) is imaged West of the MFZ, in the southward prolongation of the Limpopo Corridor (LC). By contrast, as the eastern extremity, the crust is <10 km thick when reaching the MB. Crustal velocities reveal low velocity gradients, with atypical high velocities, increasing to 7.3 to 7.6 km/s at the base of the crust, and globally in the whole crust in the LC, just West of the MFZ. We interpreted the velocity architecture combined with the evidence of volcanism at shallower depths as indicative of an intensively intruded continental crust in the NNV, and discuss the particular segmentation of the longest profile (MZ1) in the kinematic context of both divergent and strike-slip segments offshore Mozambique.

Combining wide-angle and reflection seismic observations along these two profiles and the other MOZ3/5 lines, the data shows a coherent segmentation of the E-W crustal architecture off South Mozambique. These results along MZ1 and MZ2 profiles, combined with the previously published profiles, gives a 3D-view of the NNV, which becomes one of the most passive margins covered in the world by deep wide-angle seismic data.

### Highlights

► The basement of North Natal Valley is of continental nature. ► The E-W crustal segmentation off South Mozambique images 2 areas of thinning: the main one occurred in the Limpopo Corridor. ► Our reconstruction and results coincide with the expectations of the geologists of the pan-African East Gondwana.

**Keywords** : Mozambique Channel, North Natal Valley, Sedimentary and crustal architecture, Coincident wide-angle and marine multichannel profiles, Margin formation, Lower continental crust

## 1. Introduction

The aims of Pamela MOZ35 wide-angle experiment was to answer to questions that are still matter of debate: the architecture, the nature and position of the first oceanic crust, the link with the Lebombo mountains and MCP, the ages of volcanism, the geodynamic evolution and the timing.

Indeed, as already stressed in companion papers (e.g., Thompson et al., 2019 ; Moulin et al., 2020; Aslanian et al., 2021 ; Evain et al., 2021 ; Leprêtre et al., 2021 ; Li et al., 2021, Watremez et al., 2021 ; Schnurle et al., 2023), the crustal nature in the area was the subject of a vigorous debate. Many authors, based on potential fields studies and kinematic models, have interpreted the crust in the NNV, either as thickened oceanic crust (e.g., Ludwig et al., 1968; Green 1972; Klausen, 2009; Leinweber and Jokat, 2011; Mueller & Jokat, 2019; Tikku et al., 2002; Watts, 2001) either and/or thinned continental crust (Dingle & Scrutton, 1974; Lafourcade, 1984; Domingues et al., 2016; Hanyu et al., 2017) with high magmatic content based on scarce seismic data, potential field data, and/or geological correlation with the conjugate Antarctic margin. The crustal structure of these passive margins, is important in particular 1) to understand the transition between the strike-slip margin related to the (Oxfordian-Kimmeridgian) Africa-Antarctica breakup (East Limpopo) (Evain et al., 2021; Watremez et al., 2021; Roche et al., 2021) and the pull-apart divergent margin (NNV) (Leprêtre et al., 2021; Schnurle et al., 2023) which ended with the Valanginian Africa-South America breakup when the withdrawal of the Falkland-Malvinas Plateau was accommodated by dextral strike-slip movement along the Agulhas-Falkland Fracture Zone (e.g. Thompson et al., 2019; Mueller and Jokat, 2019); 2) to study the rifting evolution of the margin from the Lebombo monocline to the continent/ocean boundary along the Mozambique FZ and 3) to better constrain kinematic reconstructions of the Africa-Antarctica-South America breakup. Indeed, exact timing and mechanisms of Gondwana breakup remain still speculative, due to the lack of quality geological and geophysical data, and difficulties in interpreting magnetic anomalies along the margins. In the absence of modern deep seismic investigation, information on the age and nature of the underlying crust, their spreading regimes and constraints on first horizontal movements are still debated. Those uncertainties have resulted in varied data interpretations and model predictions based on different data sets, leading to diverse “tight-fit” reconstructions: for example König and Jokat, 2006, Eagles and König, 2008 ; Torsvik et al., 2012 ; Gaina et al., 2013 ; Nguyen et al., 2016 ; Davis et al., 2016) adopt a model pre-dominantly based on geophysical data (gravity and magnetic data); whereas the modeling of Tarling, 1972 and Powell et al., 1980 is based on onshore geological data, with less consideration of geophysical data. Thompson et al., 2019 summarize all these comparisons and finally propose a new fit.

## 2. Geological & Tectonic Background

Located in the south-east corner of Southern Africa, the Southern Mozambique Basin is an area flanked on the west and the north-west by pre-Palaeozoic structures: the Kaapvaal and the Zimbabwe Cratons, respectively (Figure 1b). The external limits of this basin are defined by the succession of the north–south Lebombo monocline and the north-east to south-west Mateke-Sabi monocline (Salman & Abdulla, 1995). New deep seismic data acquired within the scope of the PAMELA project, provides key arguments for the existence of a thick continental crust in the MCP and NNV, in continuity to the cratons that were surrounding before the breakup, and which present a comparable velocity structure (Moulin et al., 2020 ; Leprêtre et al., 2021) . Evain et al., (2021), Li et al., (2021) and Watremez et al., (2021) detailed the Limpopo Margin (LM), eastward the MCP and the NNV, as an N–S strike-slip margin segmented by two major structures (LF and MFZ). The thinning domain reveals a continental nature in direct eastward prolongation of the continental crust that floors westwards, capped by pre-Neocomian volcano-sedimentary basin (Evain et al., 2021 ; Schnurle et al, 2023). In-between the LF and MFZ and before reaching the oceanic crust in the Mozambique Basin (MB), the Limpopo Corridor (LC) presents a domain of anomalous crust interpreted as a ductile shearing domain made of flowing lower continental crust intruded by intense magmatism (Evain et al., 2021; Figure 2). The crustal thickness is extremely variable (5 to 15 km) and appears thicker to the south (MZ1) than to the north (MZ3, MZ4, MZ5). The LC is marked by high positive gravity anomalies in continuation of those produced by the Dana and Galathea Volcanic Plateaus. For that reason, these gravity anomalies were previously thought to be a part of volcanic Mozambique Ridge (for instance: Mueller & Jokat, 2017). Recent studies have shown however that these anomalies mark in fact the presence of large and thick contourite structures above a thin continental, intruded crust (Moulin et al, 2020; Evain et al, 2021; Li et al, 2021; Babonneau et al., 2022)

## 3. Data Acquisition & Processing

### 3.1. The MOZ3/5 Experiment

The MOZ3-5 cruise of the integrated multidisciplinary PAMELA (PASSive Margin Exploration Laboratory), conducted by TOTAL, IFREMER, in collaboration with Université de Bretagne Occidentale, Université Rennes 1, Université Pierre and Marie Curie, CNRS et IFPEN, is located in the south-east corner of Southern Africa. New geophysical and geological data was acquired onboard the R/V *Pourquoi Pas?*, from February 11<sup>th</sup> to April 4<sup>th</sup> 2016, on the southern-Mozambique and Limpopo margin (Figure 1a & 1b). Seven coincident wide-angle seismic (WAS) and Multi-Channel Seismic (MCS - 720 traces) profiles were collected with 193 deployments of Ocean Bottom Sismometers



(OBS) from Ifremer's Marine Geosciences pool (Auffret et al., 2004), as well as gravimetric, magnetic, bathymetric, cored, dredged, sub-bottom profiles and water column data (Moulin and Aslanian, 2016; Moulin and Evain, 2016). Simultaneously, 124 Land Seismic Stations (LSS) were deployed in Mozambique, extending six of those profiles on land for about 100 km in order to provide information on the onshore-offshore transition (Figures 1 and 2). The seismic source was composed of 15 airguns providing a total volume of 6500-in<sup>3</sup>, with a shot interval set at 60 s. Along MZ1 and MZ2 profiles presented here, a total of respectively 3241 and 11792 air-gun shots were generated and recorded jointly by OBS, LSS and a marine streamer. 38 OBSs spaced every ~12.5 km were deployed along the 545 km long WNW-ESE oriented MZ1 profile, at water depths of 210 to 4560 m. 110 km northwards and parallel to the MZ1, MZ2 is 300km long and covered by 33 OBSs at water depths of 385 to 2022 m. Inland, 16 and 19 LSS (Reftek 125A-01 and L-4C) were deployed along MZ1 and MZ2, respectively, at altitudes ranging from 5 to 144 m. Inter-station distance of 5 km results in a landward extension of these profiles of about 100 km for MZ1 and 120 km for MZ2.

### 3.2. MCS Data Processing

The MZ1 and MZ2 profiles were acquired without any major problem. A first quality control and pre-processing was undertaken on the reflection seismic data using the *SISPEED* software (Ifremer), and further processing of the MCS data was then performed using the *GEOCLUSTER* software (CGG Veritas). The processing sequence was composed of geometry, wide butterworth frequency filter (2-12-64-92 Hz), resample traces from 2 ms to 4 ms, spherical divergence compensation, deconvolution, Common Mid Point (CMP) sorting, water-bottom multiple attenuation, frequency filter (2-12-48-64 Hz), surface-related multiple modeling and attenuation, editing and water column mute, velocity analysis, Kirchoff pre-stack time migration, update of the velocity analysis, normal move-out correction, multiple attenuation in the radon domain, dip move-out, CMP stacking, F-k migration and, Kirchoff post-stack time migration (PSTM).

### 3.3. Wide-Angle Data Processing

Pre-processing of OBS data included internal clock-drift correction to the GPS base time, and correction of instrument's positions at the seafloor using the direct water wave to take into account the drift during their descent. We applied upward and downward traveling waves separation processing (e.g. Schneider and Backus, 1964) by combining hydrophone and vertical seismometer OBS components. It includes a spiking predictive deconvolution of the upward traveling record using the downward traveling wave as signature. Spherical divergence is calculated to compensate amplitude decay of the records and traces are further scaled with a gain proportional to the offset in order to enhance the refracted events.

LSS's records were first debiased and band-pass filtered and stacked by arrays. In addition, the LSS data were reduced by an 8.0 or 8.5 km/s velocity, which flatten the principal Pn arrivals and then processed with an FX deconvolution (in a moving  $1.9 \text{ s} \times 21$  traces window) to attenuate random noise. A gain equal to the offset was finally applied to enhance the refracted events.

## 4. Data Analysis

### 4.1. Modeling approach and generalities

From the seismic data-sets presented above travel-times picks were extracted in order to build a P-wave velocity model along both MZ1 and MZ2 profiles. We applied an iterative procedure of two-dimensional forward ray-tracing using the RAYINVR software (Zelt and Smith, 1992). Modeling was performed following a layer-stripping strategy, proceeding from top (seafloor) to bottom (Moho and mantle) adjusting for each layer velocity and interface-depth nodes such as to minimize the difference between observed/picked arrival times and computed ones in the model. Initial models included a water layer where seafloor bathymetry was taken from multibeam data acquired during the MO3/5 cruise and onshore topography extracted from GEBCO. Arrival times of the main sedimentary interfaces (*see below* part 4.2.1) up to the acoustic basement (*see below* part 4.2.2) were picked from the coincident MCS line and integrated in the modeling, as long as they are correlated with identified phases in the OBS data to avoid over-parameterization of the model. We further checked the coherence of our velocity models against MCS data by converting the former from depth to two-way-travel-time (twt). Beyond the acoustic basement (*see below* parts 4.2.3 and 4.2.4), we used only arrival times picked from OBS and LSS records keeping velocity models minimal, i.e. inserting lateral topographic and velocity changes only where required by the data.

The quality of MCS data (MZ1 and MZ2) is generally good, even if seismic signal does not image beyond 2.5-3.5 s twt below the seafloor, partly due to the presence of numerous multiples from the seafloor and other major interfaces in the stratification, as well as probable high velocity layers (such as carbonate and/or volcanic layers) ([Figure 11](#)).

With respect to OBS and LSS data, their quality is also globally very good. Examples of LSS recorded sections are shown in [Figures 3 and 4](#) while some OBS records are presented in [Figures 5 to 10](#). Note that MZ2LSS06 and MZ2LSS15 to MZ2LSS20 present very noisy records probably due to poor coupling induced by the nature of the soil. Also, because MZ2LSS12 to MZ2LSS14 records were interrupted they were not used in the modeling. As for OBS records they show blind zones at shots made above the volcanic edifices of the Almirante Leite Ridge (ALR).

Based on analysis of the P-wave seismic velocity variations, the study area was subdivided into five domains:

- 1) The onshore domain of the MCP where LSS were deployed
- 2) The Continental Shelf and Slope (CSS), between -50 and 30 km model-distance on MZ1 and 0-160 km model-distance on MZ2;
- 3) the Central Domain (CD), between 40 and 270 km model-distance on MZ1 and 160 to 220 km model-distance on MZ2, dominated by the ALR;
- 4) the Limpopo Corridor (LC), at the extremity of MZ2 (230 to 260 km model-distance) and from 280 to 410 km model-distance on MZ1;
- 5) the Mozambique basin (MB) from 420 to 450 km model-distance on MZ1 only.

## 4.2 Input model setup

MZ1 velocity model is composed of 7 sedimentary and 2 volcano-sedimentary layers, 4 crustal layers and 2 mantle layers. MZ2 was modeled with 6 sedimentary layers and also 2 volcano-sedimentary layers, 4 crustal layers including a layer of anomalous high velocity separated from a single layer of mantle by a highly reflective interface (Figures 11, 12A and 13A). In the sections below, we explain how these choices were made.

### 4.2.1. Upper sedimentary and volcanic layers

Sedimentary deposits are highly heterogeneous along our two profiles with the CSS and LC representing two domains of major accumulation (Figure 11).

Over the CSS, sediments are up to 2 s twt thick but present contrasting structures and facies between profiles. On MZ1, layers S1 and S2 are poorly resolved and appear transparent. On OBS records, Ps1 refracted arrivals are observed on a very short offset range with apparent velocities round 1.6-1.7 km/s. Generally, along our profiles, Ps1 can be hard to identify due to their short offset range and low apparent velocities (1.6-1.7 km/s). The layer S1 is mainly introduced for forward modeling purposes, to allow better fit of reflected and refracted arrivals of the underlying S2 layer. S2 is better constrained by refracted arrivals with apparent velocities higher than 2.0 km/s. S3 (2.3-2.5 km/s) and S4 (2.2-2.4 km/s) highlights strong reflectors within the sedimentary sequence. The underlying S5 (2.25-2.45 km/s) and S5b (3 km/s) layers are only visible along western continental shelf where they pinch-out at 25 km and 44 km model-distance, respectively and are required by wide-angle data on the 3 last OBS (OBS36-0BS38). Finally S6 (3.25-3.75 km/s) lies directly above the bright top of the acoustic basement and presents strong internal stratification (in green on Figure 11-MZ1a). On MZ2, only 6 layers were modeled. Below the uppermost layer S1, S2 and S6 present strong internal and coherent stratification. S2 is characterized by long offset refracted phase of apparent velocity between 2.0 and 2.9 km/s with a positive gradient eastward. From MZ2OBS01 (Figure 8) to MZ2OBS07 the Ps4 refracted phase is well recorded with velocities around 3 km/s, however it becomes absent from records

further east suggesting a velocity inversion. Layer S6 is limited to the transition between the CSS and the CD and highlights high velocity, probably magmatic, lenses inter-bedded within the sedimentary sequence. On wide-angle records they show up with high apparent velocities (4.3 to 4.9 km/s) refracted phases on MZ2OBS14 -MZ2OBS16 (Figure 9).

In the CD of MZ2 profile, the two sedimentary layers of our model are strongly perturbed by volcanics from the ALR. The Ps1 apparent velocity increases to 1.85 km/s but the layer S1 pinches out between MZ2OBS17 and MZ2OBS18. The facies of S2 becomes transparent and apparent velocities on OBS sections for the Ps2 phase increase to 3.0-3.7 km/s. On MZ1 profile, the CD forms an almost flat and high plateau at the center of the NNV with the acoustic basement locally reaching the seafloor. Its topography alternates between horsts and grabbens. Sedimentary infilling within grabbens reach a maximum thickness of 1.0 s twt where three layers at most were modeled. The layers are relatively well bedded, with apparent velocity slower than CSS (around 2.0 km/s). By contrast, high velocities close to 5 km/s are recorded directly below the seafloor at the morphological high located at the intersection with the MZ6 profile

The eastern extremity of MZ2 profile reaches the LC where the sedimentary sequence thickens. Below layer S1, the interface between S2 and S3 marks a change in facies, which is almost transparent in S2 while clear and continuous stratification are visible in S3 (Figure 11-MZ2). Velocities here are mostly constrained from MZ2OBS23 (Figure 10) on which Ps2 and Ps3 have respectively 2.0-2.2 km/s and 2.8 km/s apparent velocities. On MZ1, the entire sedimentary structure of the LC is imaged up the MFZ where it ends abruptly (Figure 11-MZ1b). The area was previously recognized as a host of major contourite deposits and complex tectonic history (e.g. Li et al., 2021; Babonneau et al., 2022). Five layers (S1, S3, S5, S6 and S7) were modeled and selected to highlight similar velocity ranges in the CSS (layers S2 and S4 are thus absent). On OBS data, the phases that characterized this layer appear as a fan of secondary arrivals recorded between ~4.5 and 20 km. Below S1, S3 layer corresponds to the sedimentary body between 365 and 405 km model-distance characterized by a refracted phase of 2.3 km/s apparent velocity on MZ1OBS08 to MZ1OBS05 records. Elsewhere, beneath S1, the S5 layer that extends from the eastern part of the CD is constrained by a strong undulating reflector at its roof and refracted phases of apparent velocities increasing eastward from 2.0 km/s (MZ1OBS13) up to 2.75 km/s (MZ1OBS08-MZ1OBS05). For the layer below, a Ps6 phase is identified with apparent velocities of 2.75 km/s with a local maximum of 3.0-3.1 km/s between MZ1OBS08 and MZ1OBS06. Layer S7 is draping the acoustic basement of the LC and constrained from clearly visible Ps7 refracted phases on OBS (MZ1OBS11-MZ1OBS07) sections that show apparent velocities of 3.25-3.50 km/s. In addition, all the present S layers pinch-out eastwards on the peak localized at the MZ1OBS04, associated with the MFZ.

Finally, east of the MFZ, the extremity of MZ1 runs over the MB (between 420 and 475 km model-

distance on [Figure 11-MZ1b](#)). Here sediments thickness is up to 1.25 s twt and relatively well-bedded.

#### 4.2.2. Acoustic basement and volcano-sedimentary layers

From the CSS to the MB, a pronounced high amplitude, low frequency reflector identifies the acoustic basement, except on the westernmost part of MZ1 where this signal is lost. This basement marks the top of two volcano-sedimentary layers and reaches the seafloor at two location: MZ1OBS22 and the MFZ. The upper SV1 layer still shows some internal layering although discontinuous on the MCS profiles ([Figure 11](#)). Below, SV2 appears mostly transparent because seismic signal is lost at these depths. On OBS records, because of its strong impedance contrast, reflected arrivals from the acoustic basement can be clearly identified except again on the western CSS as the reflector is absent and on few OBS records located over the LC (e.g. MZ1OBS11-MZ1OBS09). The two SV layers are also well characterized by refracted first arrivals between 5 to 20 km offsets generally and over the whole profiles. Those have apparent velocities ranging from 4 to 6 km/s going down to 3.5-4.75 on the western CSS. The SV1 layer in our models is subdivided in two (SV1a and SV1b) because locally we modeled thin layer at the acoustic basement. This is justified by the presence of shadow zones on few OBS records (e.g MZ2OBS07) suggestive of velocity inversions in the layer SV1. The contrast is less sharp between SV1 and SV2 throughout the profiles but still some reflected arrivals were identified and used to constrain the depth of this interface.

#### 4.2.3. Crystalline crustal layers

Crustal layers were solely constrained from seismic OBS and LSS data. For both profiles four layers (G1-G4) were necessary, although only three layers (G1-G3) are used in the LC and MB domains. On OBS and LSS records, crustal refracted phases are well observed continuously over long offsets, 200-215 km on average for OBS ([Figures 5 to 10](#)) and up to 480 km offsets for LSS (e.g. MZ1LSS04: [Figure 3a](#)). Arrivals from the upper crustal layer (G1) seem to have been recorded on OBS and only at LSS located close to the the coast (MZ1LSS17 to MZ1LSS21 [Figure 3b](#)). These phases show apparent velocities around 5.75-6.00 km/s on the MCP and CSS increasing eastwards to 6.25-6.75 km/s in the LC and MB. Phases associated with deeper crustal layers (G2, G3 and G4) are recorded by almost all the instruments. Their arrivals have increasing apparent velocities in the range of 6.8-7.0 km/s in layer G2, 7.0-7.1 km/s in layer G3. Apparent velocities for layer G4 are higher than 7.0 and can reach 7.5 km/s. The corresponding refracted phases including some secondary arrivals are less evident on records.

Despite limited velocity jumps between crustal layers, reflected phases (PgP) are numerous on LSS and OBS records, which clearly suggests important internal layering. To avoid adding complexity in our models we did not exploit all these arrival times limiting the number of interfaces, which are thus

only partly sampled.

#### 4.2.4. Moho interface and Mantle layers

As for crustal phases, the reflected phase at the Moho (PmP) and reflected arrivals in the mantle are clearly identified on both LSS and OBS records. The prolongation at depth of internal heterogeneity or layering within the upper mantle is attested from evidences of high amplitude package of reflections, particularly on stations close to the coast (Figures 3b and 7).

The triplication of reflected and refracted phases at the crust/mantle interface may provide clue on crustal thickness. For LSS and OBS located over the CSS it is located at offsets larger than 150 km suggesting thick crust. Toward the east, the offset distance of the crust/mantle phase triplication decreases progressively in the CD then more abruptly in the LC to reach 60 km offset (Figures 6 to 10). In the MB, triplication occurs at less than 50 km offset.

Pn refracted arrivals from the mantle are more weakly recorded on OBS than LSS; they were not identified, for instance, on all MZ2OBS records and between MZ1OBS28 to MZ1OBS18. Two refracted phases (Pn1 and Pn2) in the mantle are generally of high amplitude, where the crust becomes thinner. These phases show apparent velocities around 8.0 km/s or slightly higher.

## 5. Forward Model and Evaluation

### 5.1. Error Analysis

From MZ1 and MZ2 OBS and LSS records, we extracted 155002 and 43078 arrivals, respectively and interpreted their corresponding phases (Tables 1 and 2). Travel-time uncertainty was computed from the ratio of signal energy (in a 20 ms window) to average energy in the 68 ms preceding the signal according to Zelt and Forsyth (1994). The uncertainty ranges from 0.020 s (MZ1) - 0.025 s (MZ2) for high ratio to 0.25 s for poor ratio. Our final models explain 151455 arrival times or 98% of total picks, with a global RMS residual of 0.069 s for MZ1. For MZ2 41277 arrivals are explained or 96% of total picks, with a global RMS travel-time residual of 0.062 s. Given our uncertainties, the two models result in a normalized chi-squared of 0.591 for MZ1 and 0.43 for MZ2 (Tables 3 and 4). For both lines crustal arrivals represent more than 50% of total picks.

### 5.2 Indirect model evaluation

Interface depth node spacing as well as velocity node spacing is key to model the lateral variations of the seismic velocity with sufficient resolution, but without introducing complexity not required by the data (Zelt, 1999). Figures 12 and 13 present three indicators of model quality for MZ1 and MZ2 profiles, respectively. The top panel (Figure 12A and 13B) represents the final velocity model, indicating in thick blue lines where the interfaces are constrained by wide-angle reflections. The middle



panel (Figures 12B and 13B) represents the parameterization of the velocity models with the depth and velocity nodes, and the reflective segments at interfaces. The bottom panel (Figures 12C and 13C) shows the resolution parameter.

For both profiles, depth and velocity nodes defining the sedimentary and volcano-sedimentary are densely spaced since they are constrained and controlled by coincident MCS data. Hence, we truly started our evaluation for velocity nodes characterizing the SV2 layer. All indicators of model quality are calculated for all velocity and depths nodes in the crust and the upper mantle. Those nodes are not spaced evenly but located where they are required to allow good fit of arrivals. Thus, the overall node spacing tends to progressively increase with depth with loss of resolution by the wide-angle data. There is also a decrease of node spacing eastward where the crust becomes thinner and local variations in the structure are better appreciated. Typically, resolution matrix diagonals greater than 0.5–0.7 are said to indicate reasonably well-resolved model parameters (e.g. Lutter & Nowack 1990). The major part of the interface and velocity nodes present good resolution ( $>0.7$ ) on both profiles (Figure 12C and 13C). Resolution is poorest at the edges of our models. For MZ2 resolution decrease west of MZ2OBS01 below the MCP and CSS, and at the eastern tip epeest crustal layer (G4). The deepest mantle layer (M2) is generally parallel to the Moho with very large km node spacing in order to simply homogenize the velocity gradient in the upper mantle.

### 5.3 Uncertainty estimation using VMONTECARLO

We assess the reliability and uniqueness of our final models in the crustal and mantle layers by exploring randomly their parameter space using VMONTECARLO (Loureiro et al., 2016 ; Figures 14 and 15). Depth nodes at the top of the crust are kept fixed during the search while those defining layers G2, G3, G4 and M1 (Moho) can randomly move vertically. Velocity nodes are allowed to vary from the top of layer G1 to the base of the upper mantle layer M1. This represents a total of 115 depth nodes and 134 velocity nodes for MZ1 while there are 52 and 87 respectively on MZ2.

For MZ1, fifty thousand random models were generated with maximum velocity variations at each node of  $\pm 0.4$  km/s and maximum depth variations of  $\pm 1.0$ , 1.0, 2.5, and 3.5 km at the top of the layers G2, G3, G4 and M1 (Moho), respectively. Furthermore, to minimize computation cost, picks for crustal phases were decimated to reduce the total number of arrivals taken into account to 50,000. For MZ2 a similar number of models were generated but with maximum velocity variation at each node of  $\pm 0.5$  km/s and maximum depth variation of 1, 2, 3, and 4 km for layers G2, G3, G4 and M1, respectively. The Metropolis algorithm and adaptive variance is utilized to increase the convergence: during the first half of the exploration, a pyramidal scheme that increases in 10 steps the allowed depth and velocity variation from 20 to 100% of their maximum is implemented, in order to finely explore the model space near our final model. During the second half, the maximum variations are



only limited by the adaptive variance that targets an acceptance ratio of 23%.

MZ1 final model explains the traveltime and phase of 47,143 of the 49,337 events or 96% of total picks, with a RMS travel-time residual of 0.078 s. Furthermore, Loureiro et al., (2016) defined an additional parameter ranging between 0 and 1, the model score, that is able to report on the quality of a model through its ability to predict the observations while maintaining good statistical fit. The first quality thresholds used to establish the model ensemble (ME) was set to 75% of the final model's quality of fit (75% of the model score), together with thresholds of 80% explained picks, chi-squared lower or equal to 2.0 and RMS lower or equal to 0.095 s. Since the quality score is constructed taking the log of the chi-squared, our events individual (data driven) uncertainty was multiplied by 1.45 in order to obtain a final chi-squared close to 1. These results in a normalized chi-squared of our preferred model of 1.063, ensuring that all random model's scores are based on chi-squared larger than 1. We finally obtained a score of 0.954 for our final model.

MZ2 final model explains the travel-time and phase of 41277 events or 96% of total picks, with a normalized chi-squared of 0.43 and an RMS travel-time residual of 62 ms. Here uncertainty was double, resulting in a normalized chi-squared of preferred model of 1.175, ensuring that all random model's scores are based on chi-squared larger than 1. The first quality threshold used to establish the model ensemble (ME) is set to 75% of the final model's quality of fit, together with thresholds of 80% explained picks, 175% of the chi-squared (2.174) and 118% of the RMS (95 ms) of our final model.

For MZ1 on the 50,000 generated random models during the simulation, 46,944 models were valid (i. e. the ME), and 355 met the quality thresholds. These 355 random models were then used to build the global uncertainty map presented in [Figures 14C and D](#).

Global uncertainty maps were then generated from the 355 and 49 random models that meet predefined thresholds for MZ1 and MZ2 respectively ([Figures 14A and B](#)). Positive and negative velocity uncertainties are generally lower than +/-0.25 km/s for both profile, except in the vicinity of the Moho where contrasts are stronger. On MZ1 there is an artifact due to the presence of a pinch-out in the Moho between 350 and 470 km model-distance. On MZ2 uncertainty reaches +0.67/-0.81 km/s: exploring +/-4 km depth variations and given large velocity contrast between lower crust and upper mantle, together with the pinch out of the G4 layer at 190 km model distance, result in large velocity variations at the Moho.

Finally, vertical slices through the 50,000 random models are taken at selected locations for each profile ([Figure 15A and 15B](#)): each 1D velocity profile is plotted, color-coded according to its normalized average score. Four horizontal constant depth (10, 20, 30, 40 km) and 4 to 5 vertical constant velocities (6.3, 6.5, 6.9, 7.3, 7.9 km/s) profiles are plotted together with their respective 95% confidence bounds. Our final models (in black line on panels c in [Figure 15A-B](#)) generally follow the

orange to red valley formed by the best normalized score values, attesting of the good quality of our solution. The width of the 95% confidence velocity bound rarely exceeds  $\pm 50$  m/s. The depth bound for the lowest constant velocity profiles (6.3-6.5 km/s) is very narrow (generally less than  $\pm 500$  m although it reaches 750 m at 250 km model distance on MZ2) as the velocity gradient in the upper crust G1 is higher than in the middle and lower crust. Hence, except where the crust begins to be thinner to the East, the depth bounds are larger as the velocity gradient in the middle crust is lower than in the upper crust. This is the case for 6.8 km/s ( $\pm 0.65$  to  $\pm 1.65$  km) and 7.0 km/s ( $\pm 0.85$  to  $\pm 3.15$  km onshore) on MZ1 and for 6.9 km/s on MZ2 where the depth bound is in the  $\pm 0.5$  to  $\pm 2.0$  km range, but reaches  $\pm 4.5$  km at 55 km model distance. In the latter model, a velocity of 7.3 km/s is reached only in the G4 layer between 0 and 190 km distance, and the depth bound in this area is in the  $\pm 0.5$  to  $\pm 1.5$  km range. On MZ1, except at 250 km model offset, where it is limited due to the presence of a velocity jump around this value, the classic tendency is followed for the velocity 7.3 km/s ( $\pm 0.35$  to  $\pm 1$  km) at the locations where our preferred model reaches higher velocities in the lower crust because of similar low gradients. To the East, approaching the MFZ and the MB, the depth bounds are much lower for the crustal layer G2, and the increase of the velocity gradient in the upper part of the crust is clearly evidenced by the proximity of the light to medium blue curves at 430 km model-distance.

Regarding more specifically the crust-mantle transition, the vertical cross-sections help to evaluate the velocity found at the base of the crust, directly above velocities typically assumed to be mantellic (velocity 7.9 km/s, panels c in [Figure 15A-B](#)). At 250 km model-distance on MZ1 for example, the cross-section QR clearly shows that a velocity 7.3 km/s is not possible at the base of the crust, while a velocity 7.6 km/s is preferred, giving the highest score on the panel b). The general increase of the velocity toward the East as well as the thinning of the crust is clearly observed and well constrained by the vertical cross-sections, which show the evolution of the position in depth of the velocity jump at the Moho, through the position of the best scores calculated for the velocity 7.9 km/s and the velocities at the base of the crust.

## 6 Velocity Model & N-S Structure Of The South Mozambique Region

In order to characterize the P-wave seismic velocity variations along these two profiles, 1-D velocity-depth profiles were extracted from the velocity model at 10 km interval ([Figure 16](#)). 1-D velocity-depth profiles below the seafloor allow to discuss the properties of crust and to establish the lateral segmentation.

### 6.1 Nature of the Crust below the NNV

The analysis of the data on the MZ1 and MZ2 profiles confirms and extends to the whole NNV the previously published results (Figure 2) (Moulin et al., 2020 ; Leprêtre et al., 2021 ; Schnurle et al., 2023) .

From the Lebombos Complex to the shoreline, between -90 and -50 km model-distance, 1-D velocity-depth profiles along MZ1 and between -40 and -15 km model distance, along MZ2 were not extracted as the crust is only partially illuminated (Figure 16A and 16B). Nevertheless, the estimated resolution is good (generally lower than 0.7 (MZ2)) in the highlighted parts and the area seems to reveal the westward rise of the upper crustal interfaces toward the Lebombos Complex, as an important thinning of the sedimentary sequence and the presence of higher velocities close to the surface at the western extremity of the MZ1 profile.

In the CSS, the crust slightly thinned eastward from 34 to 31 km thick in a distance of ~20 km. The top of the crust gently deepens eastward to ~5.5 km depth onshore close to the coastline. The velocities range from 5.6-5.8 km/s at the top of the crust up to 7.3 km/s at the base (Figure 16C). At shallower levels, the sedimentary cover rapidly thins from ~2.5-3.0 km thick in the easternmost part of the CSS to less than 0.1 km or even none locally at the Central Plateau located in the center portion of the CD. The limit between the CSS and the CD segments coincides relatively well with a slope break at the continental shelf. There, the lowest unit of the sedimentary sequence as the SV series deepens toward the West, and shows when visible a well-bedded but disturbed facies in the light of the PSDM. In addition, it also locates the area of intersection with the N-S regional negative gravity anomaly (Figure 1).

In the CD, crustal velocities are generally slightly higher than in the CSS, except in the center of the area where velocities are similar (Figure 16D). The crust has a relatively constant thickness between 26 and 28 km, but presents increasing velocities on both edges of the area. In the western portion of the CD, velocities increase to 5.8-6.1 km/s at the top of the crust, whereas the lower crust reaches 7.2-7.4 km/s top-bottom velocities. In the eastern portion of the CD, velocities are lower in the upper crust, whereas top-bottom velocities in the lower crust reach 7.4-7.6 km/s. The areas of higher crustal velocities are further illustrated by the rise of deep interfaces from both edges of the CD. At shallower levels, the CD localized all the inter-bedded high velocities volcanic events (Figure 3), except one located just East of the junction with the LC where higher lower crustal velocities up to 7.6-7.5 km/s are also found at the base of the crust. Relatively high velocities (4.2-4.8 km/s top-bottom SV1 velocities) from the SV sequence outcrop at the Central Plateau, and more particularly at the location of the crossing with the MZ6 profile (Schnurle et al., 2023). On both side lower velocities (between 2.9 and 4.2 km/s) are found through SV1 below the 2 locations of clear sedimentary fillings forming sub-basins, presenting steep borders and apparent delays of reflectors at least clearly in the sedimentary sequence.

The velocity crustal structure shows that about half of the whole crust presents velocities higher than 7 km/s, increasing to 7.3 to 7.6 km/s at its base. The crust reveals also low velocity gradients in the mid- to lower crust (mainly between 0.01 and 0.03 km/s/km), whereas the upper crust G1 present a higher gradient (between 0.15 and 0.25 km/s/km) (Figure 16C-D). These high velocities suggest the presence of larger amount of intrusive material, that it is additionally highlighted through the SV layers at shallower depths. Furthermore, the importance of the magmatism in the area through the time is further illustrated by the inter-bedded high velocity volcanic sills at different levels in the stratigraphy.

Combined with the surprisingly important thickness of the crust, the crustal architecture appears rather atypical in thickness and velocities, but in agreement with the other wide-angle profiles from the Moz35 experiment acquired in the NNV (*see below* the chapter in Discussion).

Along the MZ2 profile, based on the below seafloor 1-D velocity-depth profiles (Figure 16A), we identify 3 main areas along the profile from west to east: the CSS (W-CSS and E-CSS), the ALR, and the LC.

Throughout the entire MZ2 model, only minor lateral velocity and gradient contrasts are observed between the G1, G2, and G3 crustal layers. At the base of the crust however, the G4 layer thins from 11 to 5 km thickness at the transition from W-CSS to E-CSS, and top-bottom velocity decreases from 7.7/7.8 to 7.2/7.6 km/s between -35 and -25 km and from 7.2/7.6 to 7.2/7.4 km/s between 30 and 50 km model distance. The Moho rises from 44 to 40 km depth between 20 and 70 km model distance (Figure 16C). At the ALR, the crustal thickness thins to 28 km but preserves the same velocities and gradients as the CSS. In the LC, 1-D velocity-depth profiles were not extracted west of 260 km model distance as the crust is partially or not illuminated and the resolution generally lower than 0.7. Between 250 and 280 km model distance, the crustal thickness has been reduced from 32.5 to 30.5 km in order to match the relative decrease in the gravity free-air anomaly.

## 6.2 Nature of the Crust Below the Limpopo Corridor (LC)

Further east, the whole LC zone, observable only on MZ1, marks an area of thinned crust toward the MB from 26 km to about 12 km thick over 140 km, associated with a general increase of the crustal velocities (> 6.0 km/s) and changes in the magnetic curve character.

In more details, the LC can be separated in two sub-segments, as proposed by Evain et al., (2021): the thinned continental crust (TCC) to the west and the corridor of anomalous crust (CAC) toward the east (Figures 2 and 16E, red/orange and green lines respectively). By contrast with the TCC, the CAC reveals a different structural architecture regarding the crustal thickness as the organization of

the sedimentary and SV sequences. In addition, in the CAC, the prominent contouritic structure coincides with a major positive free-air gravimetric anomaly (Li et al., 2021).

The lower crust G4 actually thins in a distance of ~100 km beneath the TCC and the western part of the CAC and is absent in its easternmost part. The same time, the top of the upper crust deepens through 3 steps from ~5 km depth at the CNNV to ~5.6 km depth at the TCC, and finally to ~7.5 km in average at the CAC, the main down-step occurring at the TCC / CAC limit. That is particularly well expressed with the geometry of the top of the SV sequence. Although both zones correspond to a domain of thinner crust, the TCC and the CAC differ in term of 1) total crustal thickness, 2) crustal velocities, and 3) sedimentary and SV architecture. In the TCC, velocities are relatively similar to that found just westwards in the C-NNV, with velocities of 5.7 to 6 km/s at the top of the crust and 7.3-7.5 km/s top-bottom velocities in the lower crust. Velocities increase to 6 km/s at the top of the crust arriving at the junction with the CAC domain. The crustal thickness decreases from 26 to 20 km with a major part of thinning in the lower crust G4. At shallower levels, the limit between the CD and the LC segments coincides with the end of the Central Plateau, between two ~40 km wide structural highs dawned by the SV sequence (Figure 11). The seafloor begins to gently deepens and the sedimentary sequence to thicken away from the CD toward the CAC. By contrast, the CAC only shows crustal velocities higher than 6 km/s (Figure 16E). Indeed, aside from the crustal thinning and the rise of the Moho, velocities are higher along the TCC increasing heading east in the crustal layers G1, G2 and G3, as well as in SV2. It is particularly well pronounced for the layer G1 which has top and bottom velocities of 6.0-6.6 km/s and 6.5-6.9 km/s, progressively increasing from the limit with the TCC to the MFZ. Conversely, velocities at the base of the crust decline to 7.4 km/s but are still relatively high. The crustal thickness decreases from 20 to 12 km with a major pinch-out of the lower crust G4 in the western part of the CAC until it disappeared eastward at 370-380 km model-distance. More broadly, all the crustal layers thins eastward along the CAC as well as the SV sequence. At shallower depths, the top of the SV sequence forms 2 relatively buried plateaus from 320 to 380 km model-distance and from 380 to 415 km model-distance, with increasing depth moving to the east before to reach the MFZ. Above, the sedimentary cover is thicker along the CAC generally greater than 2 km, and includes a prominent contouritic domain which reaches its maximal thickness of ~ 3 km where the lower crustal layer G4 disappears below the junction between the 2 plateaus. That place also coincides with a steep increase in the SV velocities particularly in SV1, from top-bottom velocities of 4.0-4.9 km/s west of the junction between the 2 plateaus forming the CAC, to 5.2-5.9 km/s to the east. Note that the MZ1 MCS also presents a major change in the seismic signature through SV1 there. Then, the MFZ coincides with the limit between the CAC and the MB. It marks a small but abrupt step in the Moho topography as at the seafloor, and a relative down-step of the basement is localized just East of a major negative peak in the magnetic anomaly along MZ1.

In the MB, the top of the basement is clearly imaged on the MZ1 MCS by a strong reflector drawing a rough topography (marked by the top of the SV sequence there [Figure 11](#)). It lies at 5.2 to 5.7 km depth, showing a small down-step at the eastern extremity of the MCS profile. Interpreting the top of the SV sequence as the top of the crust, the crustal thickness reaches a minimum there from 10 down to 8 km, with a Moho located at about 14 km depth. The velocities at the top of the crust of more or less 5 km/s reveal a significant decrease compared to what is found at the LC ([Figure 16F](#)), while the velocities at the base of the crust of 7.40-7.45 km/s remain relatively unchanged.

## 7 Discussion

Due to the lack of deep seismic data, the crustal nature of the MCP and the NNV was largely controversial and speculative, although it is crucial in the understanding of the early stages of the Gondwana break-up in plate reconstructions and in the determination of the location of continent-ocean boundary (COB) in SE Africa (see *Introduction* chapter). The present study completes the discussion on the N-S South Mozambique crustal segmentation, the crustal nature of each segment, and the position of the COB. For that purpose, velocity-depth profiles were extracted every 10 km along MZ1 and M2 profiles ([Figure 16](#)), and then compared to the compilations for Atlantic-type Oceanic Crust from Christeson et al. (2019) and for Continental Crust from Christensen and Mooney (1995).

### 7.1 Interpretation of the crustal structure

In order to discuss the [nature of the crust below the NNV](#), the 1D velocity-depth profiles extracted from these 2 models are compared with the worldwide compilations of the continental crust from Christensen & Mooney, (1995) and of the Atlantic Ocean from Christeson et al. (2019) in [Figure 16C-E](#). From the Lebombo Complex to the LC, the velocity-depth profiles show significant disparities with those of Atlantic oceanic crust: 1) the velocities at the top of the crust (5.5 to 6.5 km/s) are generally higher, 2) the crust largely thicker, with an average thickness of 29-30 km in the NNV ; this thickness in high excess of 25 km are not compatible with oceanic LIPS (Moulin et al., 2020; Lepretre et al., 2021) and 3) velocity gradients through the crust are globally very low. That makes the crustal structure in the NNV rather incompatible with normal or thickened oceanic crust. The 1D velocity-depth profiles appear more easily comparable with the worldwide compilation for continental crust from Christensen & Mooney, (1995), showing more similar thicknesses and lower velocity gradients. However, velocities along the MZ1 model are higher than those found in the compilation, as the velocity gradient in the upper crust, particularly in the LC. Velocities observed along the MZ2 profile are however 0.5 to 1 km/s higher than observed (generally) elsewhere, most particularly at its top



(Figure 16C), but at the crossing with MZ3, MZ6, and MZ7, velocity and velocity gradients are consistent (within the uncertainty bounds – Evain et al., 2021; Leprêtre et al., 2021; Schnurle et al., 2023).

For the crustal discussion in the LC (Limpopo Corridor), we compared the 1D velocity-depth profiles in the MB with the Continental Crust velocity-depth bounds from Christensen & Mooney, (1995) and the Oceanic Crust velocity-depth bounds of the Atlantic Ocean (Christeson et al., 2019) (Figure 16E). Considering the top of the crust at the position of the Top-SV modeling interface, the 1D velocity-depth profiles are very close to that found for oceanic crust in term of gradient and velocities, while the crust remains slightly thicker (8-10 km) and velocities relatively high at its base (~7.4 km/s) and crustal velocity gradients lower.

Finally, in the MB, the 1-D velocity-depth profile extracted there clearly shows high velocities close to the seafloor (> 4 km/s), and globally a sharp increase of the crustal velocities (Figure 16E-F), that suggests additional magmatism such as buried seamounts at the top of the crust.

In summary, the data of MZ1 and MZ2 profiles confirm and complete the results already published (Moulin et al., 2020; Leprêtre et al., 2021; Evain et al., 2021; Watremez et al., 2021; Schnurle et al., 2023; Babonneau et al., 2022):

1) the interpretation of the intersecting wide-angle and MCS MZ2, MZ1 and MZ6 and MZ7 profiles demonstrates a continuity of the velocity structure between MCP and NNV with a ~35–40 km thick crust of continental nature gently thinning under the South MCP and the CSS, to about ~30 km in the major part of the NNV. In the NNV, several intense magmatic activities (from Karoo to Miocene events) have contributed to modify the propriety of the crust (e.g.,  $V_p > 7.2$  km/s) (by intrusion, underplating, metamorphism, etc..., overloading the NNV crust, and generated a general increase in velocities) (Moulin et al., 2020 ; Leprêtre et al., 2021). The CD seems to localized a major magmatic intrusion including high velocities up to 7.5 km/s at the base of the crust

2) the crustal structure of the MCP and surrounding NNV shows a clear resemblance with the two conjugate cratons at the time of the Gondwana assemblage: both crustal structures estimated along the Lebombo monocline (35–38 km) (Kwadiba et al., 2003; Nguuri et al., 2001, etc) and below the Grunehogna craton in Antarctica (Hubscher et al., 1996) are similar to the one described by our results (see Moulin et al., 2020 for more details).

3) The Limpopo Corridor is an about 100km wide N-S corridor with two segments limited by deeply rooted faults: the Limpopo fault to the west and the MFZ to the east. The westward segment evidences the thinning and termination of the MCP et NNV continental crust, while towards the east, the segment presents mixed crust interpreted as exhumed/flowed lower continental crust with magmatic intrusions. They infer that strike-slip or highly oblique rifting occurred along the LM (see Evain et al.,



2021 for more details). The N–S trending positive gravity anomalies are related to the presence of contourites above this thinned intruded continental crust.

## 7.2 Impact on these results on our understanding of the Gondwana situation

Figure 17 presents a compilation of a mean crustal thickness distribution in the East Gondwana, using published wide-angle results in Africa (Kwadiba et al., 2003, Nair et al., 2006; Leinweber et al., 2013; Domingues et al., 2016; Mueller et al., 2016) and in the Antarctica (Hubscher et al., 1996, modified from Kudryavtzev et al., 1991; Baranov and Morelli, 2013) together with the Pamela-MOZ3-5 wide-angle results. In order to compare the two sides of this part of Gondwana, the compilation is resituated in the tightest kinematic reconstruction of Thompson et al. (2019) as this is the only reconstruction that does not show overlap between the thick African and Antarctic continental crusts and therefore respects the Pamela-Moz3-5 wide-angle results.

On both sides, there is very thick continental crust, from 38 km to more than 50 km, with similar velocity structure (Moulin et al. 2020; Leprêtre et al., 2021). On the African plate, the Lebombo and Mateke-Sabi monoclines delimit an area constituted by the MCP and the NNV, with a crustal thickness slightly lower (38-42km in the MCP and 25-39 km in the NNV; Lepretre et al., 2021). On the Antarctica plate, the Grunehogna craton, fringed to the east by the Maud belt, presents also a crustal thickness similar to the MCP.

In the MB, the Continental-Oceanic Boundary (COB) is located close to the coast in the Angoche Basin, in the north-eastern corner and just south the Beira continental High, where the oldest magnetic anomaly identified is dated at 155-157 Ma, in Kimmeridgian time (Mueller and Jokat, 2019). In the NNV, the COB and its associated necking zone are located at the junction between the North and South Natal Valley, south to the Naude Ridge, probably at the location of the Ariel Graben, in good agreement with the proposition of Goodlad (1986). There, the oldest anomaly in this area is supposed to be M12 (Martin et al., 1981), associated with the Valanginian southwestward motion of Patagonia plate along the Agulhas-Falkland Fracture Zone. This motion together with the SSW motion of the Antarctica plate produced a Ridge-Ridge-Ridge Triple Junction generating the Mozambique ridge (Fisher et al., 2017).

In between the two plates, the N-S LC exhibits a very narrow margin with a steep necking zone at the termination of the MCP/NNV continental crust and a central corridor of anomalous crust bounded to the east by the Mozambique fracture zone and the oceanic crust of the MB, produced by ductile shearing responsible for the thinning of the continental crust and an oceanwards flow of lower crustal material (Evain et al., 2021, this study).

Consistent with the proposition of a full extent of the Pan-African orogenic event into Gondwana (Jacobs and Thomas, 2004), the Pamela-MOZ3-5 wide-angle results suggest a continuity of the

Kaapval and Grunghena cratons and the MCP and NNV (figure 18). The Grunghena craton represents therefore on Antarctica a piece of Proto-kalahari shield, as the Sao Luis craton is a piece of the West African Shield in the equatorial Ocean (Hurley, et al., 1967; Trompette, 1994; Moulin et al., 2010). Whilst the entire East Gondwana was impacted by the Oxfordian/Kimmeridgian kinematic phase, allowing the initiation of the Somalia (Davis *et al.*, 2016) and Mozambique (König and Jokat, 2010) oceanic basins (Thompson et al., 2019), it did not produce a complete disruption within the East African Antarctic orogeny (EAAO). In the MB, the continental Beira High (Mueller *et al.*, 2016; Mueller and Jokat, 2017; Mueller and Jokat, 2019) behaves like a piece torn from Mozambique. Such microblocks are common in ‘buffer’ areas between two geodynamically different domains (for instance, the Danakil block: Sichler 1980; McClusky et al. 2010; the Jan Mayen microcontinent: Talwani & Eldholm 1977; Gaina et al. 2009; the Iberian subplate: Olivet 1996; the Santos block: Moulin et al., 2012).

Therefore, eastward of the EAAO, the Oxfordian/Kimmeridgian kinematic phase implies the initiation of oceanic crust in the two Somalia and Mozambique Basin. Westward of the EAAO, the Oxfordian/Kimmeridgian kinematic phase also impacted the MCP, the NNV, the South-African southern margins (Paton and Underhill, 2004) and the Falkland margin (Jones et al., 2019), but only producing light thinning, magmatic intrusions, subsidence and sedimentary basins, without complete break-up and oceanic basin initiation. In these areas, the oceanic spreading will only start during the Valanginian-Barremian phase, with the south-eastward motion of the Patagonia sub-plate and the opening of the South Atlantic Ocean.

## 8 Conclusions

The aims of Pamela MOZ35 wide-angle experiment was to answer to questions that are still matter of debate: the architecture, the nature and position of the first oceanic crust, the link with the Lebombo mountains and MCP, the ages of volcanism, the geodynamic evolution and the timing.

The processing and analysis of these new data show that

- The MCP is a 34-39 km thick continental block with velocities in the upper crust from 5.6 to 6.3 km/s and in the lower crust, up to 7.1 km/s. The MCP presents a W-shape basin, with strong reflectors, dated by Schnurle et al., 2023 to Kimmeridgian to Berriasian-Valanginian, younger than previously thought.
- The NNV is of the same continental nature, but 10 km thinner, with top-bottom velocities ranging from 5.8-6.1 km/s in the upper crust, to 7.2-7.6 km/s in the lower crust.
- In the CD of the NNV, the lower part of the crust exhibits velocity variations that are probably connected to mafic intrusions. The surface is impacted by volcanism (Almirante Leite Ridge)

and a plateau shape, with very few sediment on the top. The ALR is SW-NE elongated structure, with the same direction than the Beira High and the Naude Ridge

- The Naude Ridge is strictly speaking the Necking zone, followed by oceanic crust of Valanginian age (Leprêtre et al., 2021)
- To the East, the LC represents also a necking zone, with thinned continental crust. Its thickness seems to have some variation from north to south. It is fringed in the Limpopo Margin by an uplifted block and is the place of erosional processes, Mass Transport Deposits and Contourites, probably due to the conjunction of the slope produced by the uplift and the eddies (Babonneau et al., 2022).
- Our reconstruction and results coincide with the expectations of the geologists of the pan-African East Gondwana, with a good and coherent assemblage of the different tectonic blocks (like the two late Mesoproterozoic/Early Neoproterozoic mobile belts meet, and also the 600–500 Ma East African–Antarctic Orogen), suture and shear zones.

## Author Contributions

**Conceptualization:** D. Aslanian, M. Moulin

**Formal analysis:** A. Leprêtre, F. Verrier, P. Schnürle, M. Evain, D. Moocroft, S. Leroy, E. d'Acremont

**Investigation:** M. Evain, C. Corela, A. Afilhado, A. Loureiro, D. Aslanian, M. Moulin

**Methodology:** A. Leprêtre, P. Schnürle, M. Evain, P. de Clarens, J. Thompson, D. Aslanian, M. Moulin

**Project Administration:** M. Moulin, M. Evain, D. Aslanian,

**Supervision:** P. Schnürle, M. Evain, D. Aslanian, M. Moulin

**Visualisation:** A. Leprêtre, P. Schnürle, M. Evain, P. de Clarens, J. Thompson, D. Aslanian, M. Moulin

**Writing – original draft:** M. Moulin, A. Leprêtre, D. Aslanian

**Writing – review & editing:** M. Moulin, D. Aslanian, M. Evain, P. Schnürle

## Data availability:

The data of the PAMELA-MOZ3 (Moulin and Aslanian, 2016) and PAMELA-MOZ5 (Moulin and Evain, 2016) cruises are archived and referenced at SISMER and accessible on request at <https://doi.org/10.17600/16009500> and <https://doi.org/10.17600/16001600>.

## Acknowledgements:

We thank the captain, crew, and MCS technical team of the R/V Pourquoi-Pas. We also thank the OBS technical team who maintain and constantly improve our OBS pool, as well as the land stations deployment team. The PAMELA (PASSive Margins Exploration Laboratories) project was initiated in the early 2010th by TOTAL and IFREMER in collaboration with French universities (Université de Bretagne Occidentale, Université Rennes 1, Université Pierre and Marie Curie), the CNRS and the IFPEN. A Leprêtre and F. Verrier respective post-doc studies and contract were co-funded by TOTAL and Ifremer as part of the PAMELA scientific project. The GMT (Wessel and Smith, 1998), Seismic

Unix (Cohen and Stockwell, 2019; Stockwell, 1999), and Geocluster (CGG-Veritas) software packages were used extensively in this study. We thank the Editor, Ramon Carbonell, the reviewer Anouk Beniest and one other anonymous reviewer for their comments, which substantially improved the manuscript.

## References

- Aslanian, D., Moulin, M., Evain, M., Schnurle, P., 2021. Comment on 'The challenge in restoring magma-rich rifted margins: The example of the Mozambique-Antarctica conjugate margins' by Tomasi S., Kuszniir N., Manatschal G. & Despinos F., *Gondwana Research*, 103, 401-403, <https://doi.org/10.1016/j.gr.2021.10.019>.
- Auffret, Y., Pelleau, P., Klingelhoefer, F., Géli, L., Crozon, J., Lin, J.I., Sibuet, J.-C., 2004. MicrOBS : a new generation of bottom seismometer. *First Break*, 22, 41–47.
- Babonneau N., Raison F., Genêt A., Lopes U., Fierens R., Miramontes E., Révillon S., Rabineau M., Droz L., Belleney D., Aslanian D., Moulin M., in press. Contourite on the Limpopo Corridor, Mozambique margin: long-term evolution, facies distribution and Quaternary processes, accepted to *Sedimentology*
- Baranov, A. and Morelli, A., 2013. The Moho depth map of the Antarctica region. *Tectonophysics*, 609, 299–313.
- Christensen, N. I. and Mooney, W. D., 1995. Seismic velocity structure and composition of the continental crust: A global view, *J. Geophys. Res.-Sol. Ea.*, 100, 9761–9788, <https://doi.org/10.1029/95JB00259>, 1995.
- Christeson, G.L., Goff, J.A., Reece, R.S., 2019. Synthesis of oceanic crustal structure from two-dimensional seismic profiles. *Rev. Geophys.* 57, 504–529. <https://doi.org/10.1029/2019RG000641>.
- Cohen, J. and Stockwell, J. J. W., 2019. CWP/SU: Seismic Unix Release No. 44: an open source software package for seismic research and processing.
- Davis, J.K., Lawver, L.A., Norton, I.O., Gahagan, L.M., 2016. New Somali Basin magnetic anomalies and a plate model for the early Indian Ocean. *Gondwana Res.*, 34, 16–28.
- Dingle, R. V., & Scrutton, R. A., 1974. Continental breakup and the development of post-Paleozoic sedimentary basins around southern Africa. *The Geological Society of America Bulletin*, 85, 1467–1474.
- Domingues, A., Silveira, G., Ferreira, A. M., Chang, S.-J., Custódio, S., and Fonseca, J. F., 2016 Ambient noise tomography of the East African Rift in Mozambique, *Geophys. J. Int.*, 204, 1565–1578, <https://doi.org/10.1093/gji/ggv538>, 2016.
- Eagles, G., König, M., 2008. A model of plate kinematics in Gondwana breakup. *Geophys. J. Int.*, 173, 703–717.
- Evain M., P. Schnürle, A. Leprêtre, F. Verrier, L. Watremez, N. A. Dias, A. Afilhado, A. Loureiro, C. Corela, P. de Clarens, D. Aslanian, M. Moulin, 2021, Crustal structure of the East-African Limpopo Margin, a strike-slip rifted corridor along the continental Mozambique Coastal Plain and North-Natal Valley, *Solid Earth*, 12, 1865–1897, <https://doi.org/10.5194/se-2020-209>
- Fischer M.D., Uenzelmann-Neben G., Jacques G., Werner, R., 2017. The Mozambique Ridge: a document of massive multistage magmatism. *Geophysical Journal International*, 208, 449-467.
- Gaina, C., Torsvik, T., Van Hinsbergen, D., Medvedev, S., Werner, S., Labails, C., 2013. The African Plate: A history of oceanic crust accretion and subduction since the Jurassic. *Tectonophysics*. <https://doi.org/10.1016/j.tecto.2013.05.037>.<sup>[L]</sup><sub>SEP</sub>
- Gaina, C., Gernigon, L. & Ball, P. 2009. Palaeocene–Recent plate boundaries in the NE Atlantic and the formation of the Jan Mayen microcontinent. *Journal of the Geological Society*, London, 166, 601–616, doi:10.1144/0016-76492008-112.
- Goodlad, S. W. 1986. Tectonic and sedimentary history of the Mid-Natal Valley (S.W. Indian Ocean), available at: <http://hdl.handle.net/11427/23640> (last access: 10 August 2021), University of Cape Town, 1986.
- Goodlad, S. W., Martin, A. K., & Hartnady, C. J. H., 1982. Mesozoic magnetic anomalies in the southern Natal Valley. *Nature*, 295, 686–688. <https://doi.org/10.1038/295686a0>
- Green, A. G., 1972. Seafloor spreading in the Mozambique Channel. *Nature Physical Science*, 236, 19–21. <https://doi.org/10.1038/physci236019a0>
- Hanyu, T., Nogi, Y., & Fujii, M., 2017. Crustal formation and evolution processes in the Natal Valley and

- Mozambique Ridge, off South Africa. *Polar Science*, 13, 66–81. <https://doi.org/10.1016/j.polar.2017.06.002>
- Hubscher, C., Jokat, W., & Miller, H., 1996. Crustal structure of the Antarctic continental margin in the Eastern Weddell Sea. In B. C. Storey, E. C. King, & R. A. Livermore (Eds.), *Weddell Sea Tectonics and Gondwana Break-up* (pp. 165–174). 108. London, UK: Geological Society Special Publication.
- Hurley, P.M., de Almeida, F.F.M., Melcher, G.C., Cordani, U.G, Rand, J.R., Kawashita, K., Vadoros, P., Pinson, W.H., Fairbairn, H.W. Jr., 1967. Test of continental drift by comparison of radiometric ages. A pré-drift reconstruction shows matching geologic age provinces in West Africa and Northern Brazil. *Science*, 157, 495-500.
- Jacobs, J., and R. J. Thomas, 2004, Himalayan-type indenter-escape tectonics model for the southern part of late Neoproterozoic-early Paleozoic East African-Antarctic orogen, *Geology*, 32, 721–724, doi:10.1130/G20516.1.
- Jones, D., McCarthy, D.J., Dodd, T. J.H., 2019. Tectonostratigraphy and the petroleum systems in the Northern sector of the North Falkland Basin, South Atlantic. *Marine and Petroleum Geology*, 103, 150-162.
- Klausen, M.B., 2009. The Lebombo monocline and associated feeder dyke swarm; diagnostic of a successful and highly volcanic rifted margin? *Tectonophysics*, 268, 42–62.
- König, M., Jokat, W., 2006. The Mesozoic breakup of the Weddell Sea. *J. Geophys. Res.*, 111, B12102. <https://doi.org/10.1029/2005JB004035>.
- König, M., Jokat, W., 2010. Advanced insights into magmatism and volcanism of the Mozambique Ridge and Mozambique Basin in the view of new potentialfield data. *Geophys. J. Int.*, 180 (1), 158–180.
- Kudryavtzev, G.A., Butzenko, V.V. and Kadmina, I.N. 1991, Crustal section across the western Dronning Maud Land continental margin from geophysical data, in: Abstracts, Sixth international symposium on Antarctic earth sciences, pp. 330–335. National Institute for Polar Research, Tokyo.
- Kwadiba, M. T. O. G., Wright, C., Kgaswane, E. M., Simon, R. E., & Nguuri, T. K., 2003. Pn arrivals and lateral variations of Moho geometry beneath the Kaapvaal craton. *Lithos*, 71, 393–411. <https://doi.org/10.1016/j.lithos.2003.07.008>
- Lafourcade, P. (1984). *Etude géologique et géophysique de la marge continentale du sud Mozambique (17°S à 28°S)*. Thesis. Paris VI, France: Université Pierre et Marie Curie.
- Leinweber, V., Klingelhoefer, F., Neben, S., Reichert, C., Aslanian, D., Matias, L., ... Jokat, W., 2013. The crustal structure of the central Mozambique continental margin—wide-angle seismic, gravity and magnetic study in the Mozambique Channel, Eastern Africa. *Tectonophysics*, 599, 170–196. <https://doi.org/10.1016/j.tecto.2013.04.015>
- Leinweber, V., & Jokat, W., 2011. Is there continental crust underneath the northern Natal Valley and the Mozambique Coastal Plains? *Geophysical Research Letters*, 38, 87–101. <https://doi.org/10.1029/2011gl047659>
- Leprêtre A., P. Schnürle, M. Evain, F. Verrier, D. Moorcroft, P. de Clarens, N. Dias, A. Afilhado, A. Loureiro, S. Leroy, E. d'Acremont, D. Aslanian, M. Moulin, 2020. Deep structure of the North Natal Valley, from the Mozambique Coastal Plain to the Naude Ridge, using combined wide-angle and reflection seismic data, *Journal of Geophysical Research*, <https://doi.org/10.1029/2020JB021171>.
- Li, H., Tang, Y., Moulin, M., Aslanian, D., Evain, M., Schnürle, P., Leprêtre, A., and Li, J., 2021. Seismic evidence for crustal architecture and stratigraphy of the Limpopo Corridor: New insights into the evolution of the sheared margin offshore southern Mozambique, *Mar. Geol.*, 435, 106468, <https://doi.org/10.1016/j.margeo.2021.106468>, 2021.
- Loureiro A., A. Afilhado, L. Matias, M. Moulin, & D. Aslanian, 2016. Monte Carlo approach to assess the uncertainty of wide-angle layered models: Application to the Santos Basin, Brazil. *Tectonophysics*, 683, 286– 307. <https://doi.org/10.1016/j.tecto.2016.05.040>
- Ludwig, W. J., Nafe, J. E., Simpson, E. S. W., and Sacks, S., 1968. Seismic-refraction measurements on the Southeast African Continental Margin, *J. Geophys. Res.*, 73, 3707–3719, <https://doi.org/10.1029/JB073i012p03707>.
- Lutter W. J., and R. L. Nowack, 1990. Inversion for crustal structure using reflections of the PASSCAL Ouachita experiment, *Geophysical Journal International*, 95, 4633-4646.
- Martin, A. K., Hartnady, C. J. H., & Goodlad, S. W., 1981. A revised fit of South America and South Central Africa. *Earth and Planetary Science Letters*, 54, 295–305. [https://doi.org/10.1016/0012-821X\(81\)90012-1](https://doi.org/10.1016/0012-821X(81)90012-1)
- McClusky, S., Reilinger, R. et al. 2010. Kinematics of the southern Red Sea–Afar Triple Junction and implications for plate dynamics. *Geophysical Research Letters*, 37, L05301, doi: 10.1029/2009GL041127.



- Moulin, M. and Aslanian, D., 2016. PAMELA-MOZ03 cruise, RV Pourquoi pas?, <https://doi.org/10.17600/16001600>, 2016.
- Moulin, M. and Evain, M., 2016. PAMELA-MOZ05 cruise, <https://doi.org/10.17600/16009500>, 2016.
- Moulin, M., Aslanian, D., Evain, M., Leprêtre, A., Schnurle, P., Verrier, F., Thompson, J., Clarens, P. D., Leroy, S., and Dias, N., 2020. Gondwana breakup: Messages from the North Natal Valley, *Terra Nova*, 32, 205–214, <https://doi.org/10.1111/ter.12448>, 2020.
- Moulin, M., Aslanian, D., Rabineau, M., Patriat, M., Matias, L., 2012. Kinematic keys of the Santos – namibe basins. In: Mohriak, W.U., Danforth, A., Post, P.J., Brown, D.E., Tari, G.C., Nemcok, M., Sinha, S.T. (Eds.), *Conjugate Divergent Margins. Geological Society, London, Special Publications*. <https://doi.org/10.1144/SP369.3>.
- Moulin, M., Aslanian, D. & Unternehr, P. 2010. A new starting point for the history of the Equatorial and South Atlantic. *Earth-Science Reviews*, 98, 1–37.
- Mueller, C.O., & Jokat, W., 2017. Geophysical evidence for the crustal variation and distribution of magmatism along the central coast of Mozambique. *Tectonophysics*, 712–713, 684–703. <https://doi.org/10.1016/j.tecto.2017.06.007>
- Mueller C., O. & W. Jokat, 2019. The initial Gondwana break-up: A synthesis based on new potential field data of the Africa-Antarctica Corridor, *Tectonophysics*, 750, 301–328.
- Mueller, C.O., Jokat, W. and Schreckenberger, B., 2016, The crustal structure of Beira High, central Mozambique—Combined investigation of wide-angle seismic and potential field data. *Tectonophysics*, 683, 233–254.
- Nair, S. K., Gao, S. S., Liu, K. H., & Silver, P. G., 2006. Southern African crustal evolution and composition: Constraints from receiver function studies. *Journal of Geophysical Research: Solid Earth*, 111, B02304. <https://doi.org/10.1029/2005jb003802>
- Nguuri, T. K., Gore, J., James, D. E., Webb, S. J., Wright, C., Zengeni, T. G.,... Kaapvaal Seismic Group, 2001. Crustal structure beneath southern Africa and its implications for the formation and evolution of the Kaapvaal and Zimbabwe cratons. *Geophysical Research Letters*, 28, 2501–2504. <https://doi.org/10.1029/2000g1012587>
- Nguyen, L.C., Hall, S.A., Bird, D.E., Ball, P.J., 2016. Reconstruction of the East Africa and Antarctica continental margins. *J. Geophys. Res. Solid Earth*, 121, 4156–4179. <https://doi.org/10.1002/2015JB012776>.
- Olivet, J.-L. 1996. Kinematics of the Iberian Plate. *Bulletin des Centres de Recherches Exploration–Production Elf Aquitaine*, 20, 131–195.
- Paton, D., A. & Underhill, J., R., 2004. Role of crustal anisotropy in modifying the structural and sedimentological evolution of extensional basins: the Gamtoos Basin, South Africa, *Basin Research*, 16, 339–359, doi: 10.1111/j.1365-2117.2004.00237.x
- Powell, C., Johnson, B.D., Veevers, J.J., 1980. A revised fit of east and west Gondwanaland. *Tectonophysics*, 63, 13–29. [https://doi.org/10.1016/0040-2851\(80\)90003-9](https://doi.org/10.1016/0040-2851(80)90003-9)
- Roche, V., Leroy, S., Guillocheau, F., Revillon, S., Rufet, G., Watremez, L., et al., 2021. The Limpopo magmarich transform margin (South Mozambique) – Part 2: Implications for the Gondwana breakup. *Tectonics*. <https://doi.org/10.1029/2021TC006914>
- Ryan, W. B. F., Carbotte, S. M., Coplan, J. O., O'Hara, S., Melkonian, A., Arko, R., et al., 2009, Global Multi-Resolution Topography synthesis, *Geochemistry, Geophysics, Geosystems*, 10, Q03014. <https://doi.org/10.1029/2008GC002332>
- Salman, G. & I. Abdulla, 1995. Development of the Mozambique and Ruvuma sedimentary basins, offshore Mozambique. *Sediment. Geol.*, 96, 7–41. <http://dx.doi.org/10.1016/0037-0738>.
- Sandwell D. T. and Smith, W. H. F., 2009, Global marine gravity from retracked Geosat and ERS-1 altimetry: Ridge segmentation versus spreading rate, *Journal of Geophysical Research*, 114 (B1), B01411, doi:10.1029/2008JB006008.
- Schneider W.A. & M. Backus, 1964. Ocean-bottom seismic measurements off the California coast, *Journal of Geophysical Research*, 69(6) 1135–1143.
- Schnurle, P., Leprêtre, A., Evain, M., De Clarens, P., Thompson, J., Dias, N., Afilhado, A., Loureiro, A., Leroy, S., d'Acremont, E., Aslanian, D. & Moulin, M., 2023. Crustal structure and stratigraphy of the South Mozambique Margin to Mozambique Ridge from combined wide-angle and reflection seismic and drill hole data. Accepted in *Earth and Space Science*.
- Sichler, B., 1980. La bielle Danakil, un modèle pour l'évolution géodynamique des Afars. *Bulletin de la Société Géologique de France*, 22, (6), 925–932.
- Stockwell, J. W., 1999. The CWP/SU: Seismic Unix package, *Comput. Geosci.*, 25, 415–419.
- Talwani, M. & Eldholm, O., 1977. Evolution of the Norwegian–Greenland Sea. *Geological Society of America*

*Bulletin*, 88, 969–999, doi: 10.1130/0016-7606.

- Tarling, D.H., 1972. Another Gondwanaland. *Nature*, 238, 92–93. <sup>[1]</sup><sub>SEP</sub>
- Thompson J. O., M. Moulin, D. Aslanian, F. Guillocheau, P. de Clarens, 2019. New starting point for the Indian Ocean: Second phase of breakup for the Gondwana, *Earth-Science Reviews*, 191, 26-56.
- Tikku, A.A., Karen, M., Marks, K.M., Kovacs, L.C., 2002. An Early Cretaceous extinct spreading center in the northern Natal valley. *Tectonophysics*, 347, 87–108.
- Torsvik, T., Van der Voo, R., Preeden, U., Mac Niocaill, C., Steinberger, B., Doubrovine, P.V., van Hinsbergen, D.J.J., Domeier, M., Gaina, C., Tohver, E., Meert, J.G., McCausland, P.J.A., Cocks, L.R.M., 2012. Phanerozoic polar wander, palaeogeography and dynamics. *Earth Sci. Rev.*, 114, 328–365.
- Trompette, R., 1994. Geology of Western Gondwana 2000–500 Ma: Pan-African-Brasiliano aggregation of South America and Africa. A. A. Balkema, Rotterdam, Brookfield. pp. 350.
- Watremetz L., S. Leroy, E. d'Acremont, V. Roche, A. Leprêtre, F. Verrier, D. Aslanian, N.A. Dias, A. Afilhado, A., P. Schnürle, R. Castilla, F. Despinos, M. Moulin, 2021; The Limpopo magmatic transform margin (South Mozambique) – Part 1: insights from deep-structure seismic imaging. *Tectonics*, 40, e2021TC006915. doi.org/10.1029/2021TC006915.
- Watts, A. B., 2001. Gravity anomalies, flexure and crustal structure at the Mozambique rifted margin, *Mar. Petrol. Geol.*, 18, 445–455, [https://doi.org/10.1016/S0264-8172\(00\)00079-9](https://doi.org/10.1016/S0264-8172(00)00079-9).
- Wessel, P. and Smith, W. H. F., 1998. New, improved version of Generic Mapping Tools released, *EOS Trans. Amer. Geophys. U.*, 79, 579.
- Zelt, C. A., & Forsyth, D. A., 1994. Modeling wide-angle seismic data for crustal structure: Southeastern Grenville province. *Journal of Geophysical Research*, 99, 11687–11704. <https://doi.org/10.1029/93JB02764>
- Zelt C.A. & R.B. Smith, 1992. Seismic travel time inversion for 2-D crustal velocity structure, *Geophysical Journal International*, 108, 16-34.
- Zelt C. A., 1999, Modelling strategies and model assessment for wide-angle seismic traveltimes data, *Geophysical Journal International*, 183-204.

## Captions

Figure 1 : Location of the wide-angle seismic MZ1 and M2 profiles of the PAMELA MOZ3/5 experiment, South Mozambique. Inset: schematic cartoon that simplifies the geodynamic evolution of the area (a) on topographic (GMRT grid, Ryan et al., 2009) and bathymetric (GEBCO) map. The gray stars indicated the location points of 1D Vs-depth profiles from Domingues et al., 2016. (b) on free-air gravity anomaly (Sandwell & Smith, 2009). The main features known in the area are from Mueller and Jokat (2019), which are based on Leinweber and Jokat (2012) and Mueller and Jokat (2017) for the magnetic spreading anomalies in the Mozambique Basin, and on Goodlad et al. (1982) for the magnetic anomalies in the South Natal Valley. The outline of the Naude Ridge, the South and East Tugela Ridges are from Goodlad (1986). OBS and LSS locations from the MOZ3/5 experiment are indicated by circle and triangle, respectively. Stations along the MZ1 and MZ2 profiles are indicated in red, except those presented in the following article that are highlighted in yellow. AG, Ariel Graben; DP, Dana Plateau; E-TuR, East Tugela Ridge; GP, Galathea Plateau, Vauban Plateau; MG, Mazenga Graben; NNV, North Natal Valley; NR, Naude Ridge; SNV, South Natal Valley; S-TuR, South Tugela Ridge.

Figure 2 : Map of the main segmentation and boundaries area resulting from the combined interpretation of PAMELA-MOZ35 deep seismic profiles, modified from Evain et al., 2021. Pink lines are locations of line drawings of commercial MCS profiles used by Evain et al., 2021 and Schnürle et al., in press. The background shows the main geological units and structures on land: KC stands for Kaapval Craton, LB stands for Lebombo monocline, MSM stands for Mateke Sabi Monocline, MCP stands for Mozambique Coastal Plain, NNV stands for North Natal Valley, and ZC stands for Zimbabwe Craton. Offshore bathymetric contours in the LM are as follows: Limpopo margin (LM), Mozambique Basin (MB) and South Natal Valley (SNV). The main geological features are as follows: Continental Shelf and Slope (CSS), Central Domain (CD), Central Plateau (CP), Almirante Leite Ridge (ALR), Beira continental block or high (BH), Limpopo Fault (LF), Mozambique Ridge (MR), Mozambique Fracture Zone (MFZ), Tugela and Naude ridges, and Ariel Graben (AG). MOZ35 seismic acquisition in the NNV and LM is shown in red, with MZ1 and MZ2 profiles highlighted with a bold red line.

Figure 3 : Left : MZ1LSS04 – Focus on the crust and mantle at positive offsets (toward the E). a) Seismic record; b) Seismic record with color coded predicted travel-times overlain; c) Color coded synthetic; d) Color coded observed travel-times (vertical bars, the size showing the uncertainty range), overlain by color coded predicted travel-times (color dots); e) Seismic rays. On a, b, c, and d, travel-times is reduced by a velocity of 8.0 km/s. Right : MZ1LSS20 – Focus on the crust and mantle at positive offsets (toward the E). a) Seismic record; b) Seismic record with color coded predicted travel-times overlain; c) Color coded synthetic; d) Color coded observed travel-times (vertical bars, the size showing the uncertainty range), overlain by color coded predicted travel-times (color dots); e) Seismic rays. On a, b, c, and d, travel-times



is reduced by a velocity of 8.0 km/s.

Figure 4 : Left : MZ2LSS01 – Focus on the crust and mantle at positive offsets (toward the E). a) Seismic record; b) Seismic record with color coded predicted travel-times overlain; c) Color coded synthetic; d) Color coded observed travel-times (vertical bars, the size showing the uncertainty range), overlain by color coded predicted travel-times (color dots); e) Seismic rays. On a, b, c, and d, travel-times is reduced by a velocity of 8.0 km/s. Right : MZ2LSS20 – Focus on the crust and mantle at positive offsets (toward the E). a) Seismic record; b) Seismic record with color coded predicted travel-times overlain; c) Color coded synthetic; d) Color coded observed travel-times (vertical bars, the size showing the uncertainty range), overlain by color coded predicted travel-times (color dots); e) Seismic rays. On a, b, c, and d, travel-times is reduced by a velocity of 8.0 km/s.

Figure 5 : MZ1OBS32 – Focus on the crust and mantle at both negative and positive offsets. a) Seismic record; b) Seismic record with color coded predicted travel-times overlain; c) Color coded synthetic; d) Color coded observed traveltimes (vertical bars, the size showing the uncertainty range), overlain by color coded predicted travel-times (color dots); e) Seismic rays; f) MCS time migrated section and color coded model interfaces. On a, b, c, and d, travel-times is reduced by a velocity of 7.0 km/s.

Figure 6 : MZ1OBS15 – Focus on the crust and mantle at both negative and positive offsets. *Same legend and colour code as Figure 5.*

Figure 7 : MZ1OBS02 – Focus on the crust and mantle at both negative and positive offsets. *Same legend and colour code as Figure 5.*

Figure 8 : MZ2OBS01 – Focus on the crust and mantle at both negative and positive offsets. *Same legend and colour code as Figure 5.*

Figure 9 : MZ2OBS16 – Focus on the crust and mantle at both negative and positive offsets. *Same legend and colour code as Figure 5.*

Figure 10 : MZ2OBS23 – Focus on the crust and mantle at both negative and positive offsets. *Same legend and colour code as Figure 5.*

Figure 11 : Insert of MOZ3/5 dataset (blue lines), MZ1 and MZ2 profiles are indicated by red lines. OBS and LSS locations are indicated by white circles. A) two-way travel-time record section of MCS data along MZ2 profile overlain by time converted interfaces of wide-angle model MC2, B) Zoom on the western part of the two-way travel-time record section of MCS data along MZ1 profile overlain by time converted interfaces of wide-angle model MC1. C) Zoom on the eastern part of the two-way travel-time record section of MCS data along MZ1 profile overlain by time converted interfaces of wide-angle model MC1. Vertical exaggeration at seafloor is 1:7.5.

Figure 12 : Final velocity model for the MZ1 profile and evaluation of the wide-angle model. (a) Final MZ1 velocity model. Thick blue lines indicate interfaces constrained by wide-angle reflections. Shaded areas indicate ray-coverage. (b) Model parameterization, including interface depth nodes (squares), top and bottom layer velocity nodes (red circles). Interfaces where reflections have been observed on OBS/LSS data are highlighted in blue. (c) Resolution of velocity (gridded and colored) and depth nodes (colored squares). Zones that were not imaged are blanked. MCP, Mozambique Coastal Plain; NNV, North Natal Valley.

Figure 13 : Final velocity model for the MZ2 profile and evaluation of the wide-angle model. (a) Final MZ2 velocity model. Thick blue lines indicate interfaces constrained by wide-angle reflections. Shaded areas indicate ray-coverage. (b) Model parameterization, including interface depth nodes (squares), top and bottom layer velocity nodes (red circles). Interfaces where reflections have been observed on OBS/LSS data are highlighted in blue. (c) Resolution of velocity (gridded and colored) and depth nodes (colored squares). Zones that were not imaged are blanked. MCP, Mozambique Coastal Plain; NNV, North Natal Valley.

Figure 14 : A-B: Global uncertainty map generated from the stander deviation of the 49 random models meeting our thresholds. Crust and mantel portion of our final wide-angle model MZ2. (A) Positive velocity uncertainty. (B) Negative velocity uncertainty. The hashed areas indicate the standard deviation of the depth of the interfaces explored during Vmontecarlo. Same legend in C-D for MZ1 profile, generated from the stander deviation of the 355 random models meeting our thresholds.

Figure 15 : A-Evaluation of the wide-angle model MZ2 through the normalized average scores distribution at 250, 185, 120, 55, -10 and -75 km model-distance. (b) Normalized average model scores distribution. Black line indicates the final velocity model. Thin dashed black envelope indicates the exploration domain of independent parameter uncertainties. Colored lines mark the location of horizontal (constant depth, letters A to H) and vertical (constant velocity, letters K–V)

cross-sections of the average model scores presented in (a) and (c) respectively. Thick black dashlines on (a) and (c) indicate the 95% of confidence level, that is, 95% of the normalized average score. Same legend in B for MZ1 profile, through the normalized average scores distribution at 430, 350, 250, 150, 50 and -50 km model-distance

Figure 16 : Insert of MOZ3/5 dataset (blue lines), MZ1 and MZ2 profiles are indicated by red lines. OBS and LSS locations are indicated by white circles. Comparison of the 1-D velocity-depth profiles (1D velocity profiles) extracted from the final P-waves velocity models for different domains along the MZ1 (b) and MZ2 (a) profiles with compilations from the literature. Distribution of the 1-D velocity-depth profiles extracted and presented in (c) - (f). The color-code is according to the segmentation along MZ1 and MZ2. (c) Comparison of the 1D velocity profiles extracted in the CSS with the compilation for Continental Crust (CC) from Christensen & Mooney, 1995. (d) Comparison of the 1D velocity profiles extracted in the CD with the compilation for Continental Crust (CC) from Christensen & Mooney, 1995. (e) Comparison of the 1D velocity profiles extracted in the LC with the compilation for Continental Crust (CC) from Christensen & Mooney, 1995 and (f) Comparison of the 1D velocity profiles extracted in the MB with the compilation for Oceanic Crust from Christeson et al., 2019. CSS, Continental Shelf & Slope; CD, Central Domain ; LC, Limpopo Corridor ; TCC, Thinned Continental Crust ; CAC, corridor of anomalous crust ; MB, Mozambique Basin ; MFZ, Mozambique Fracture Zone.

Figure 17 : Zooming on the tightest kinematic reconstruction of Thompson et al. (2019), with a compilation of a mean crustal thickness distribution in the East Gondwana, using published wide-angle results in Africa (Kwadiba et al., 2003, Nair et al., 2006; Leinweber et al., 2013; Domingues et al., 2016; Mueller et al., 2016) and in the Antarctica (Hubscher et al., 1996, modified from Kudryavtzev et al., 1991; Baranov and Morelli, 2013) together with the Pamela-MOZ3-5 wide-angle results (Moulin et al., 2020; Leprêtre et al., 2021; Evain et al., 2021; Watremez et al., 2021; Schnurle et al., 2023; this study). AB, Angoche Basin; AG, Ariel Graben; MCP, Mozambique Coastal Plain; NNV, North Natal Valley; NR, Naude Ridge; SNV, South Natal Valley; LC, Limpopo Corridor.

Figure 18 : Revised geodynamic map of NNV and neighbouring areas in a Gondwana reconstruction, modified from Jacobs and Thomas, 2004, on the base of Pamela-MOZ3-5 wide-angle results (Moulin et al., 2020; Leprêtre et al., 2021; Evain et al., 2021; Watremez et al., 2021; Schnurle et al., 2023; this study).

Table 1 : summarizes reflected or refracted phase name, number of explained events, residual mean-square, and normalized chi-squared value for MZ1 profile

Table 2 : summarizes reflected or refracted phase name, number of explained events, residual mean-square, and normalized chi-squared value for MZ2 profile

Table 3: summarizes the instrument name, distance along model, direction code (-1 for rays traveling westward and 1 traveling eastward), number of explained events, travel-time residual mean-square, and normalized chi-squared value, respectively for MZ1

Table 4 summarizes the instrument name, distance along model, direction code (-1 for rays traveling westward and 1 traveling eastward), number of explained events, travel-time residual mean-square, and normalized chi-squared value, respectively for MZ2

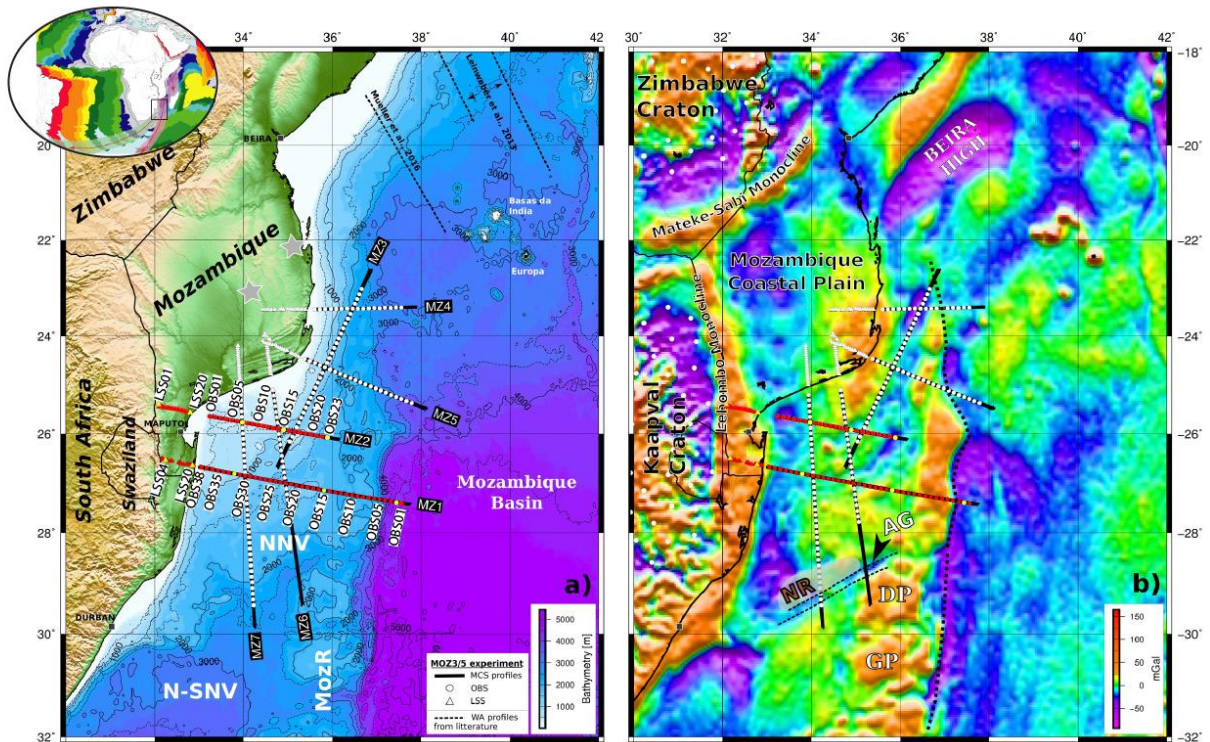


Figure 1

Figure 1 : Location of the wide-angle seismic MZ1 and M2 profiles of the PAMELA MOZ3/5 experiment, South Mo-zambique. Inset: schematic cartoon that simplifies the geodynamic evolution of the area (a) on topographic (GMRT, Ryan et al., 2009) and bathymetric (GEBCO) map. The gray stars indicated the location points of 1D Vs-depth profiles from Domingues et al., 2016. (b) on free-air gravity anomaly (Sandwell & Smith, 2009). The main features known in the area are from Mueller and Jokat (2019), which are based on Leinweber and Jokat (2012) and Mueller and Jokat (2017) for the magnetic spreading anomalies in the Mozambique Basin, and on Goodlad et al. (1982) for the ma-gnetic anomalies in the South Natal Valley. The outline of the Naude Ridge, the South and East Tugela Ridges are from Goodlad (1986). OBS and LSS locations from the MOZ3/5 experiment are indicated by circle and triangle, respectively. Stations along the MZ1 and MZ2 profiles are indicated in red, except those presented in the following article that are highlighted in yellow. AG, Ariel Graben; DP, Dana Plateau; E-TuR, East Tugela Ridge; GP, Galathea Plateau, Vauban Plateau; MG, Mazenga Graben; NNV, North Natal Valley; NR, Naude Ridge; SNV, South Natal Valley; S-TuR, South Tugela Ridge.

Figure 2 : Map of the main segmentation and boundaries area resulting from the combined interpretation of PAMELA-MOZ35 deep seismic profiles, modified from Evain et al., 2021. Pink lines are locations of line drawings of commercial MCS profiles used by Evain et al., 2021 and Schnurle et al., in press. The background shows the main geological units and structures on land: KC stands for Kaapval Craton, LB stands for Lebombo monocline, MSM stands for Mateke Sabi Monocline, MCP stands for Mozambique Coastal Plain, NNV stands for North Natal Valley, and ZC stands for Zimbabwe Craton. Offshore bathymetric contours in the LM are as follows: Limpopo margin, Mozambique Basin (MB) and South Natal Valley (SNV). The main geological features are as follows: Continental Shelf and Slope (CSS), Central Domain (CD), Central Plateau (CP), Almirante Leite Ridge (ALR), Beira continental block or high (BH), Limpopo Fault (LF), Mozambique Ridge (MR), Mozambique Fracture Zone (MFZ), Tegula and Naude ridges, and Ariel Graben (AG). MOZ35 seismic acquisition in the NNV and LM is shown in red, with MZ1 and MZ2 profiles highlighted with a bold red line.

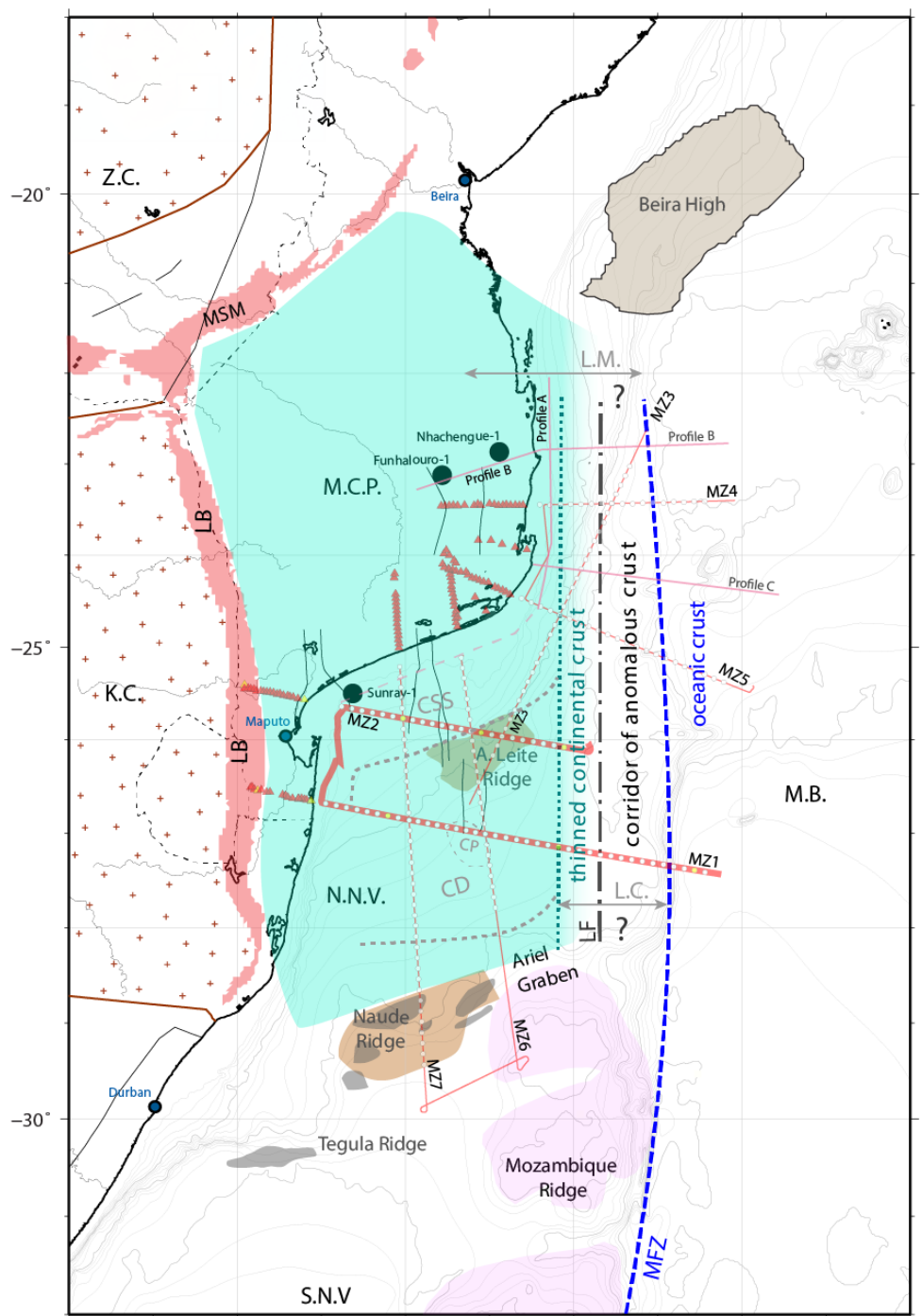


Figure 2



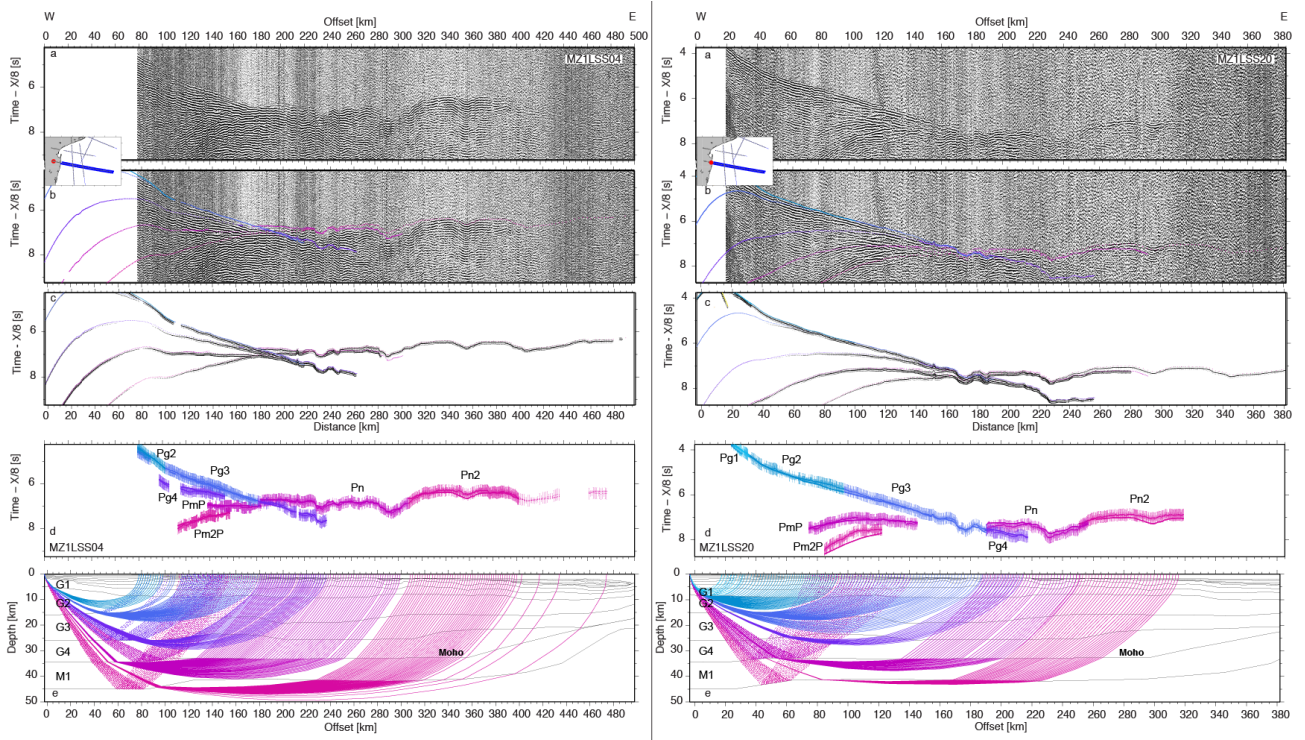


Figure 3 : Left : MZ1LSS04 – Focus on the crust and mantle at positive offsets (toward the E). a) Seismic record; b) Seismic record with color coded predicted travel-times overlain; c) Color coded synthetic; d) Color coded observed travel-times (vertical bars, the size showing the uncertainty range), overlain by color coded predicted travel-times (color dots); e) Seismic rays. On a, b, c, and d, travel-times is reduced by a velocity of 8.0 km/s. Right : MZ1LSS20 – Focus on the crust and mantle at positive offsets (toward the E). a) Seismic record; b) Seismic record with color coded predicted travel-times overlain; c) Color coded synthetic; d) Color coded observed travel-times (vertical bars, the size showing the uncertainty range), overlain by color coded predicted travel-times (color dots); e) Seismic rays. On a, b, c, and d, travel-times is reduced by a velocity of 8.0 km/s.

Figure 3

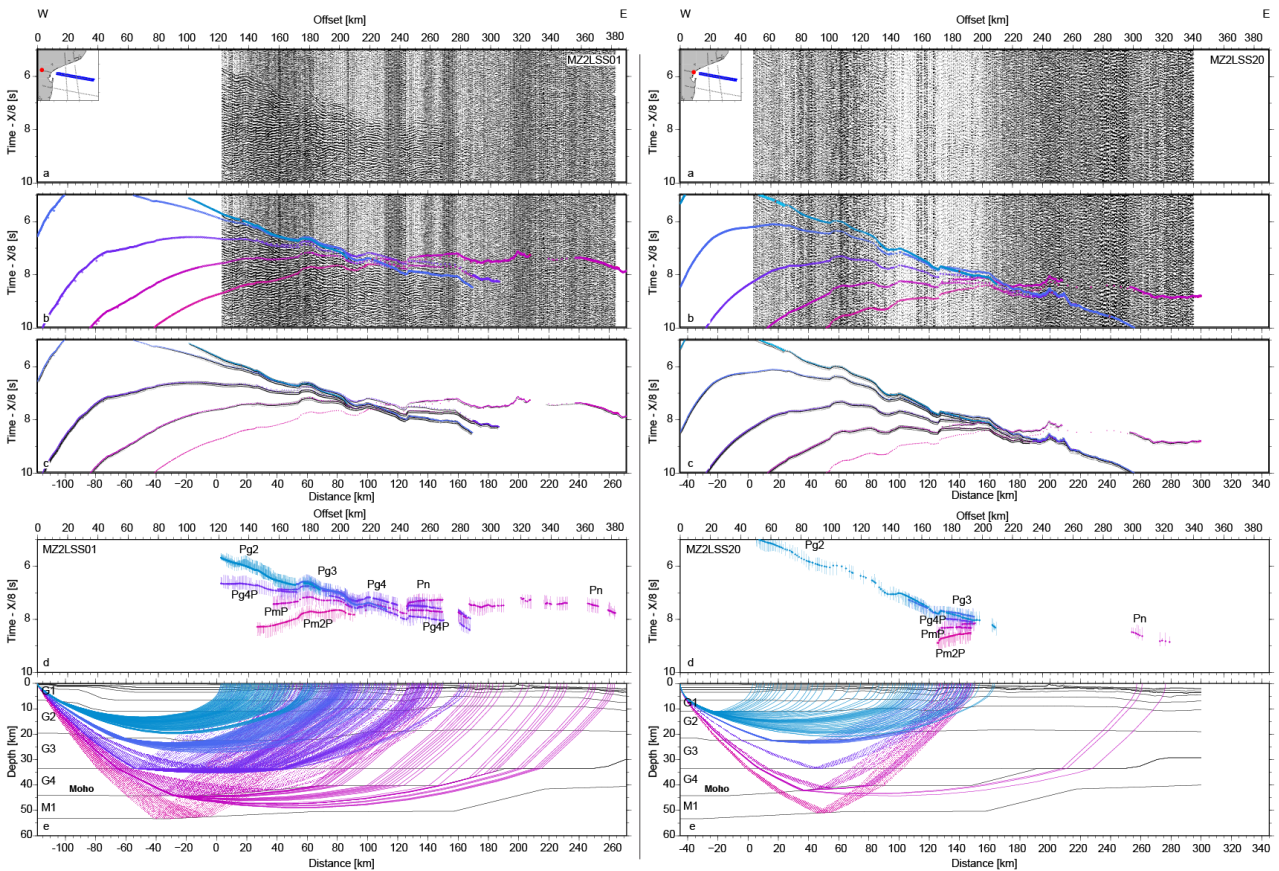


Figure 4: Left : MZ2LSS01 – Focus on the crust and mantle at positive offsets (toward the E). a) Seismic record; b) Seismic record with color coded predicted travel-times overlain; c) Color coded synthetic; d) Color coded observed travel-times (vertical bars, the size showing the uncertainty range), overlain by color coded predicted travel-times (color dots); e) Seismic rays. On a, b, c, and d, travel-times is reduced by a velocity of 8.0 km/s. Right : MZ2LSS20 – Focus on the crust and mantle at positive offsets (toward the E). a) Seismic record; b) Seismic record with color coded predicted travel-times overlain; c) Color coded synthetic; d) Color coded observed travel-times (vertical bars, the size showing the uncertainty range), overlain by color coded predicted travel-times (color dots); e) Seismic rays. On a, b, c, and d, travel-times is reduced by a velocity of 8.0 km/s.

Figure 4

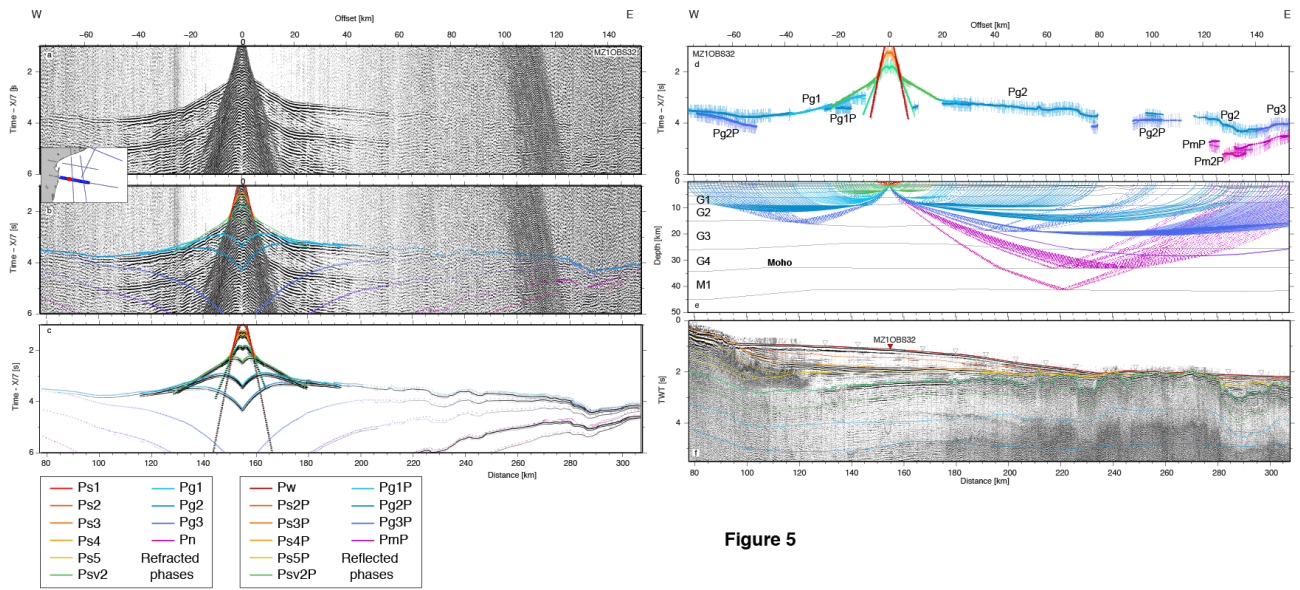


Figure 5

Figure 5 : MZ1OBS32 – Focus on the crust and mantle at both negative and positive offsets. a) Seismic record; b) Seismic record with color coded predicted travel-times overlay; c) Color coded synthetic; d) Color coded observed traveltimes (vertical bars, the size showing the uncertainty range), overlay by color coded predicted travel-times (color dots); e) Seismic rays; f) MCS time migrated section and color coded model interfaces. On a, b, c, and d, travel-times is reduced by a velocity of 7.0 km/s.

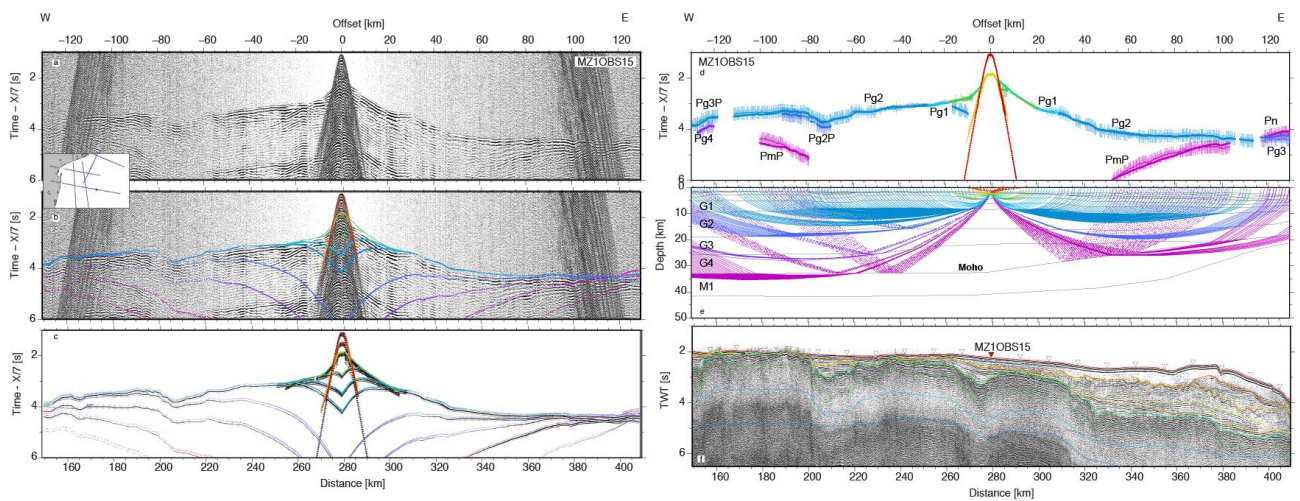


Figure 6

Figure 6 : MZ1OBS15 – Focus on the crust and mantle at both negative and positive offsets. Same legend and colour code as Figure 5.



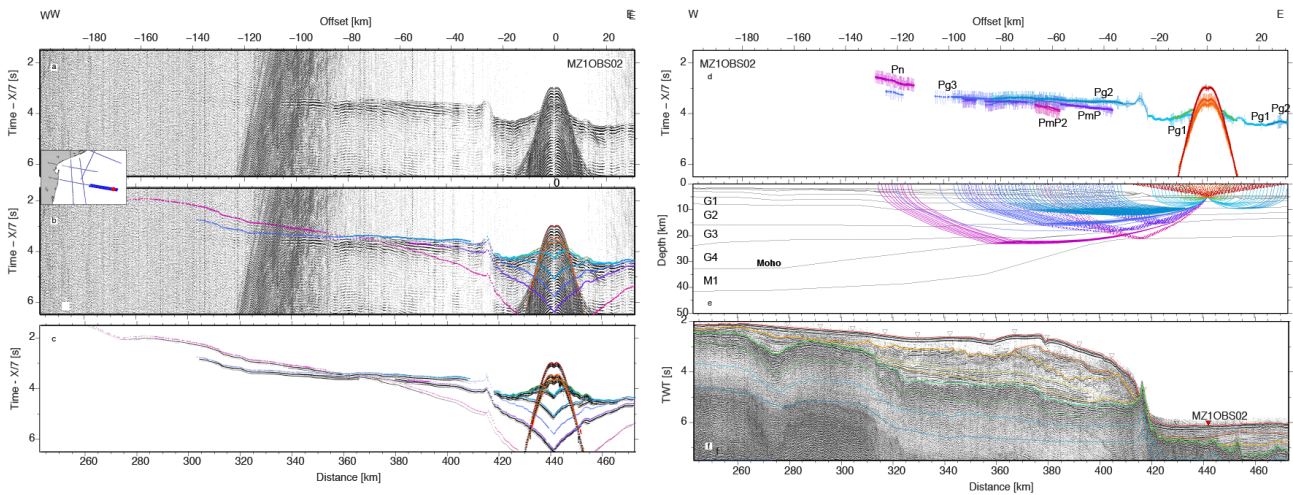


Figure 7 : MZ1OBS02 – Focus on the crust and mantle at both negative and positive offsets. Same legend and colour code as Figure 5.

Figure 7

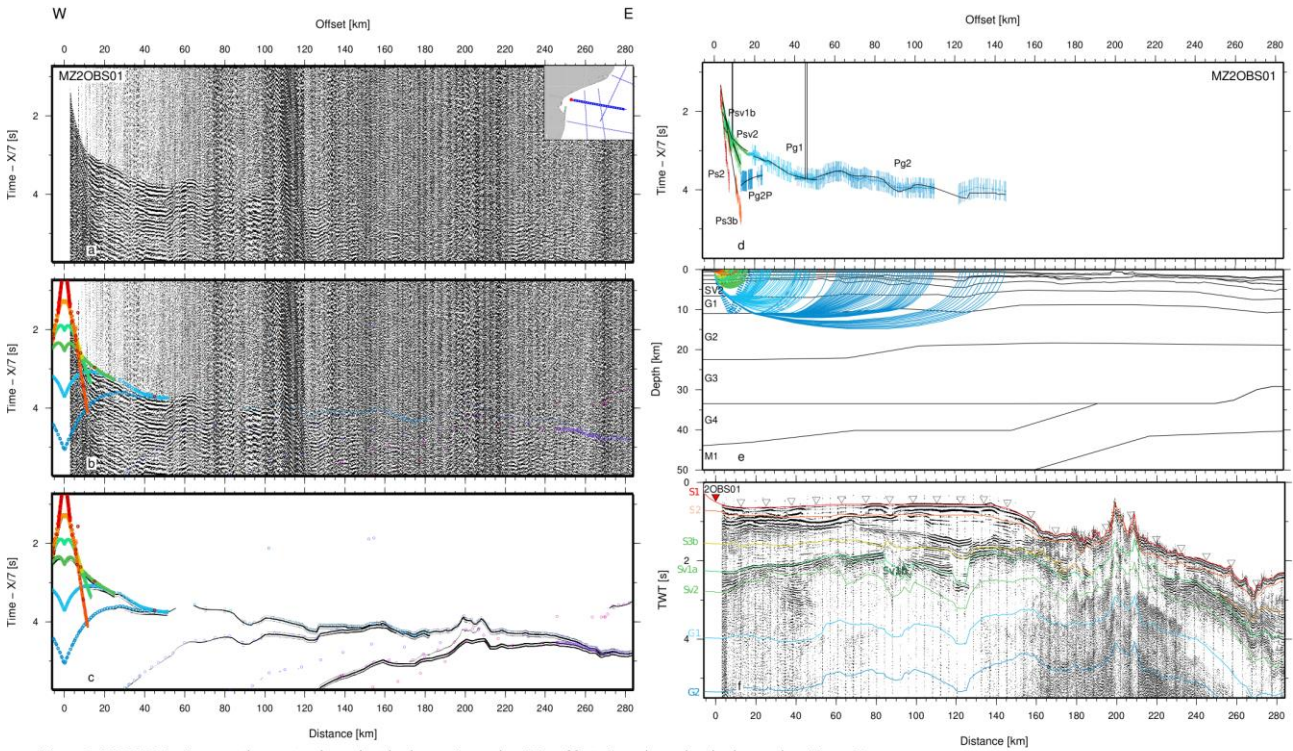


Figure 8 : MZ2OBS01 – Focus on the crust and mantle at both negative and positive of fsets. Same legend and colour code as Figure 5.

Figure 8



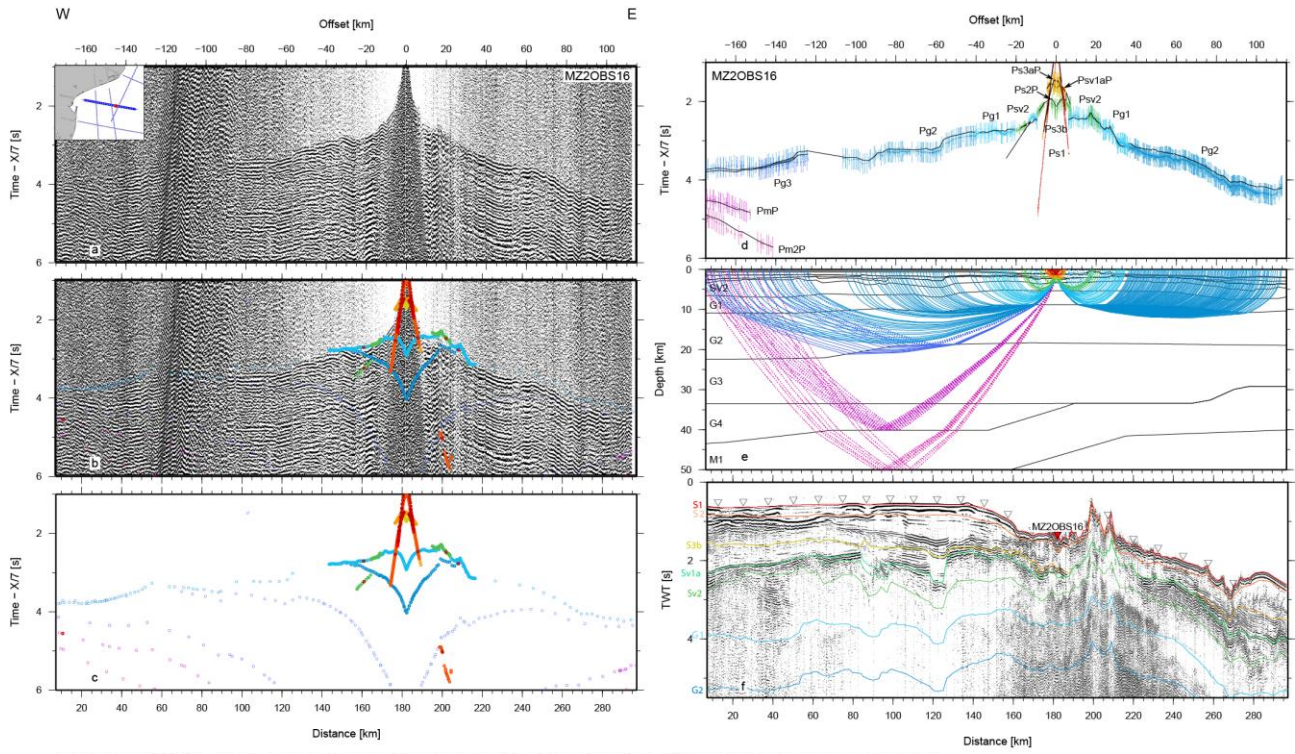


Figure 9 : MZ2OBS16 – Focus on the crust and mantle at both negative and positive offsets. Same legend and colour code as Figure 5.

Figure 9

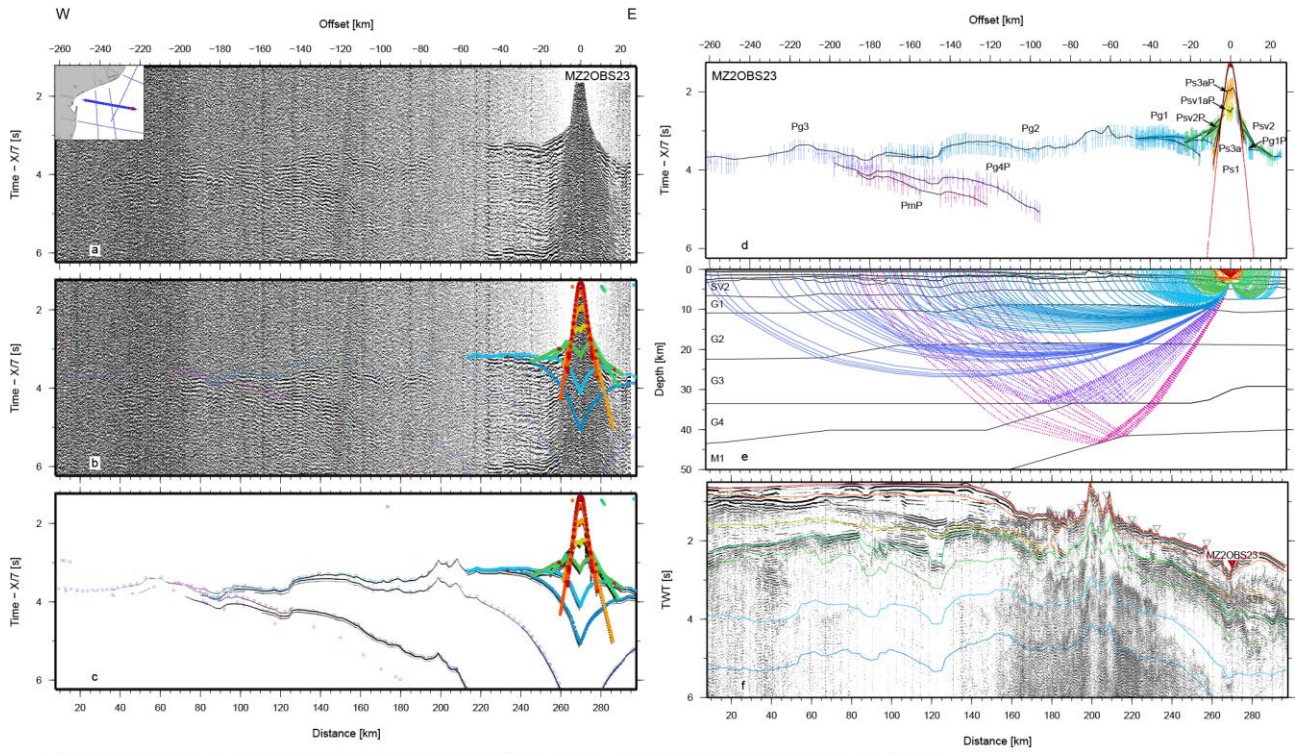
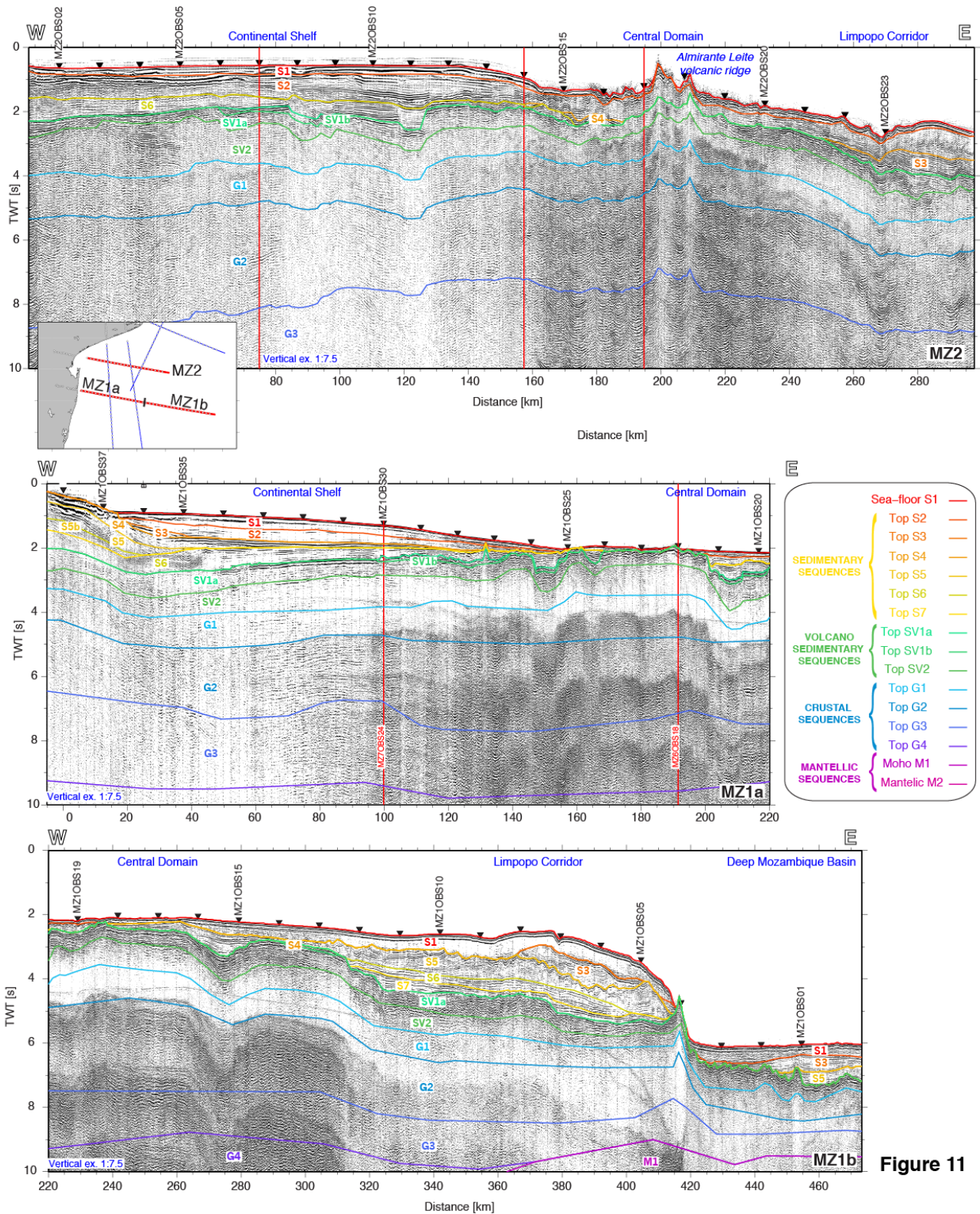


Figure 10 : MZ2OBS23 – Focus on the crust and mantle at both negative and positive offsets. Same legend and colour code as Figure 5.

Figure 10





**Figure 11**

Figure 11 : Insert of MOZ3/5 dataset (blue lines), MZ1 and MZ2 profiles are indicated by red lines. OBS and LSS locations are indicated by white circles. A) two-way travel-time record section of MCS data along MZ2 profile overlain by time converted interfaces of wide-angle model MC2, B) Zoom on the western part of the two-way travel-time record section of MCS data along MZ1 profile overlain by time converted interfaces of wide-angle model MC1. C) Zoom on the eastern part of the two-way travel-time record section of MCS data along MZ1 profile overlain by time converted interfaces of wide-angle model MC1. Vertical exaggeration at seafloor is 1:7.5.

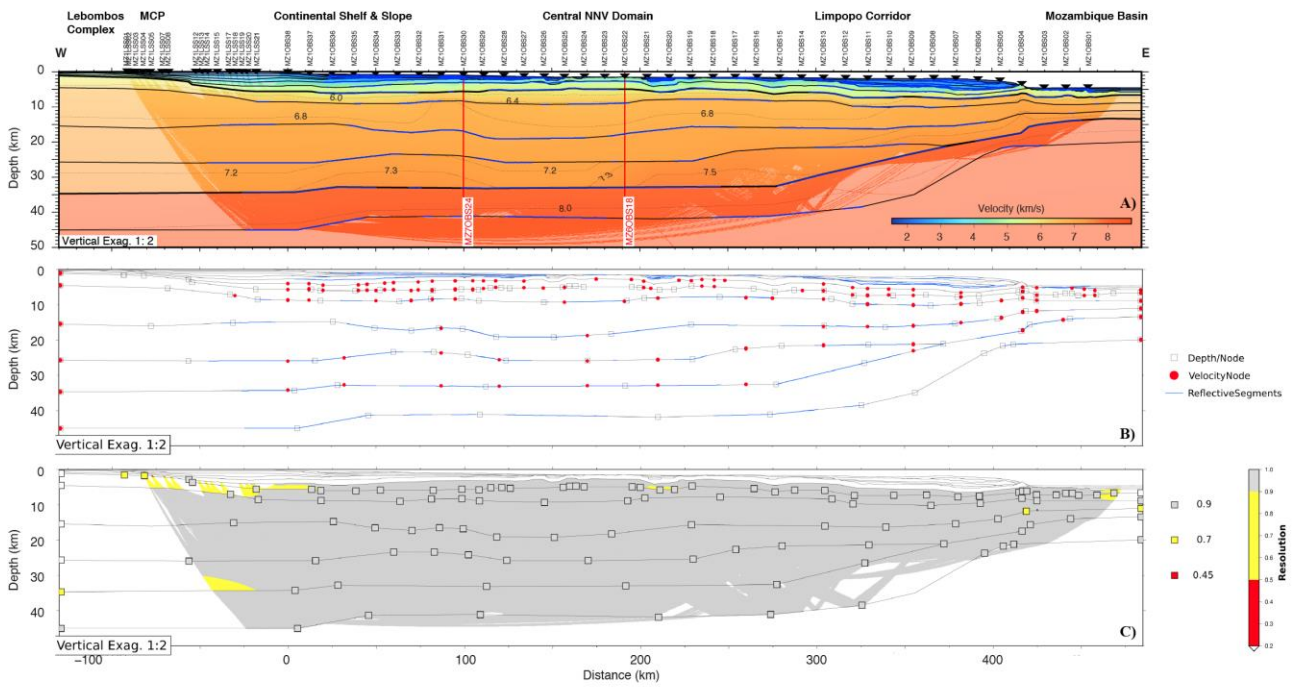


Figure 12

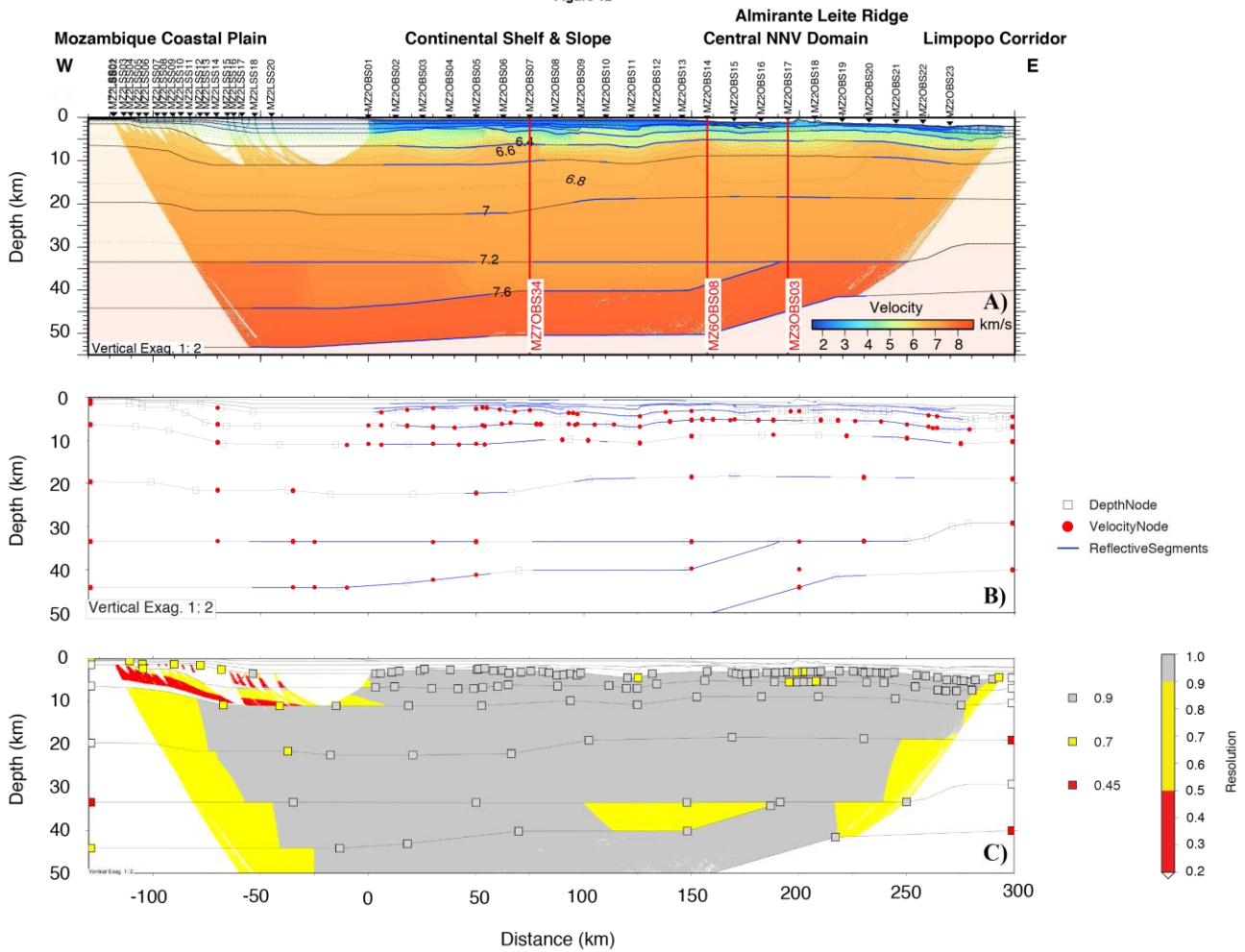
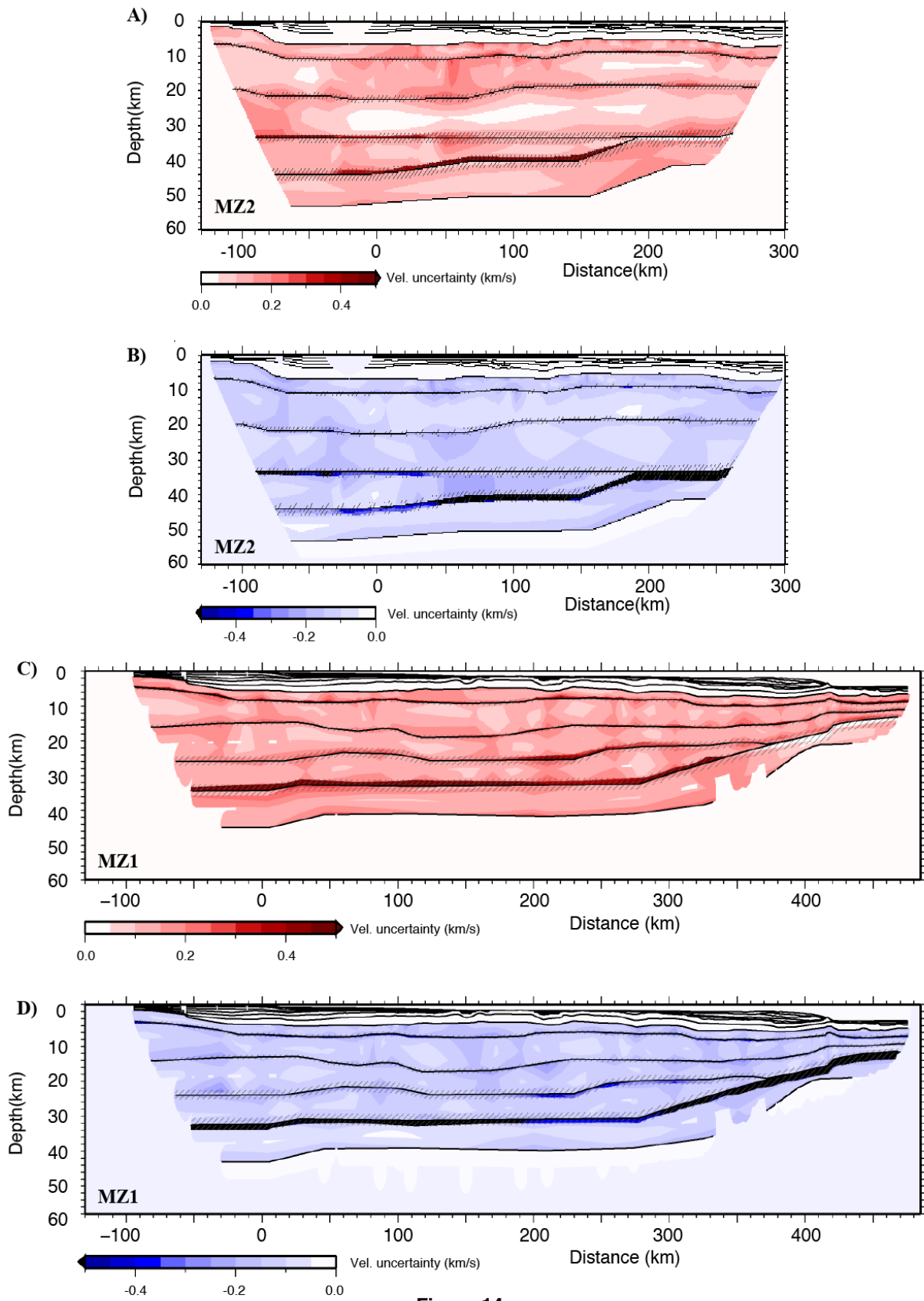


Figure 13





**Figure 14**

Figure 14 : A-B: Global uncertainty map generated from the stander deviation of the 49 random models meeting our thresholds. Crust and mantel portion of our final wide-angle model MZ2. (A) Positive velocity uncertainty. (B) Nega-tive velocity uncertainty. The hashed areas indicate the stander deviation of the depth of the interfaces explored during Vmontecarlo. Same legend in C-D for MZ1 profile, generated from the stander deviation of the 355 random models meeting our thresholds.



**A) MZ2**

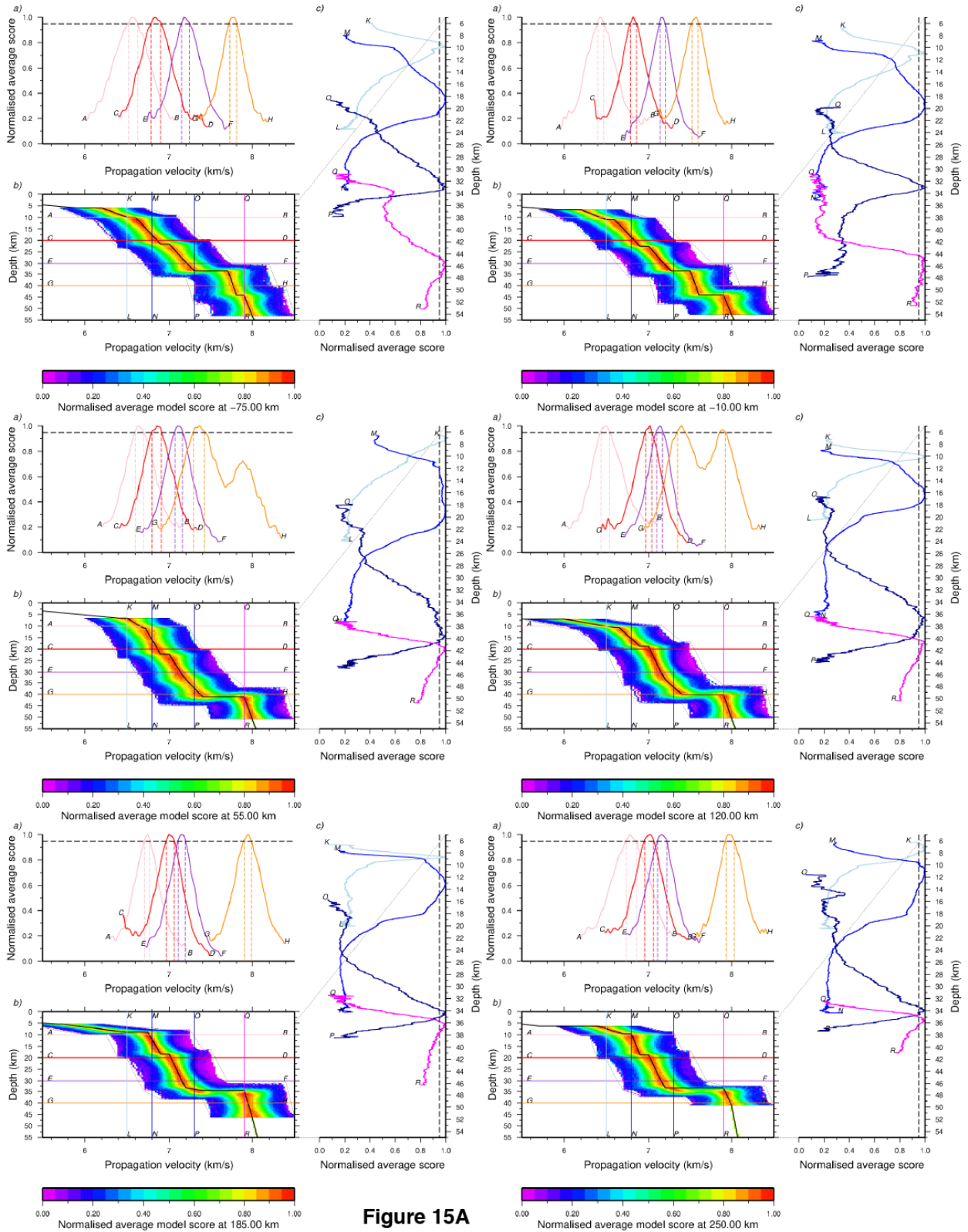


**Figure 15A**

Figure 15 : A-Evaluation of the wide-angle model MZ2 through the normalized average scores distribution at 250, 185, 120, 55, -10 and -75 km model-distance. (b) Normalized average model scores distribution. Black line indicates the final velocity model. Thin dashed black envelope indicates the exploration domain of independent parameter uncertain-ties. Colored lines mark the location of horizontal (constant depth, letters A to H) and vertical (constant velocity, letters K–V) cross-sections of the average model scores presented in (a) and (c) respectively. Thick black dashlines on (a) and (c) indicate the 95% of confidence level, that is, 95% of the normalized average score.

**B) MZ1**

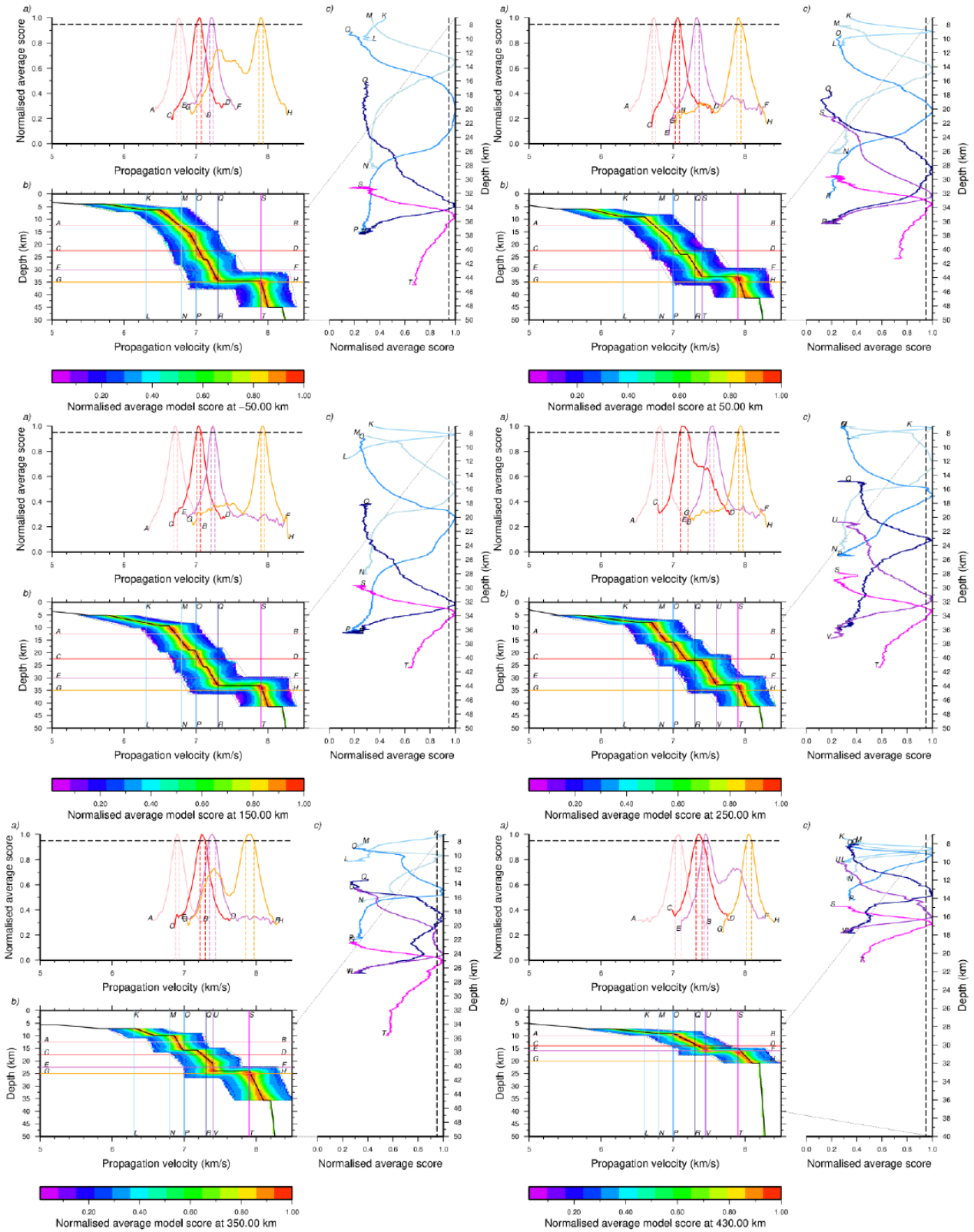


**Figure 15B**

Figure 15b: Same legend in B for MZ1 pro-file, through the normalized average scores distribution at 430, 350, 250, 150, 50 and -50 km model-distance

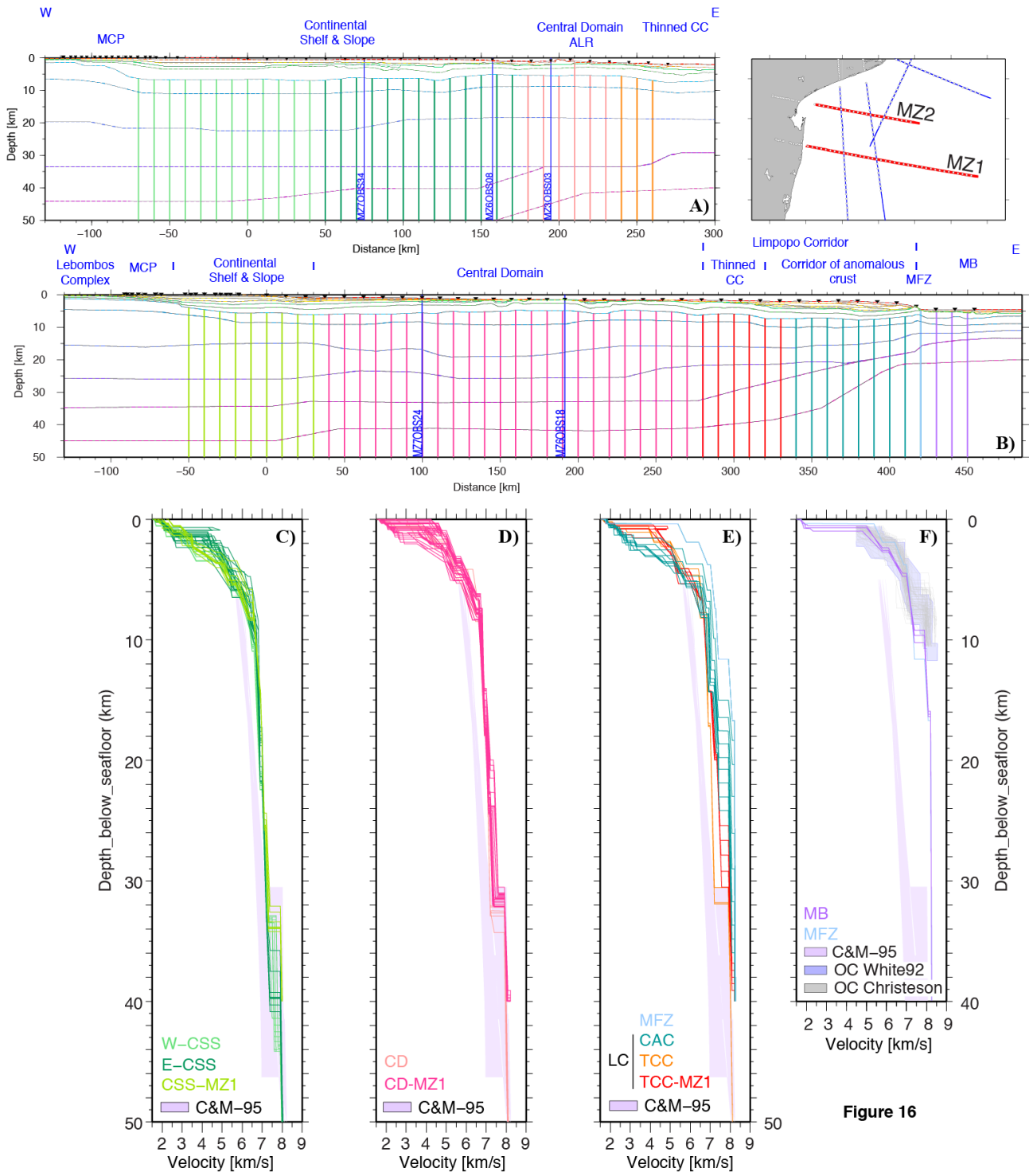


Figure 16

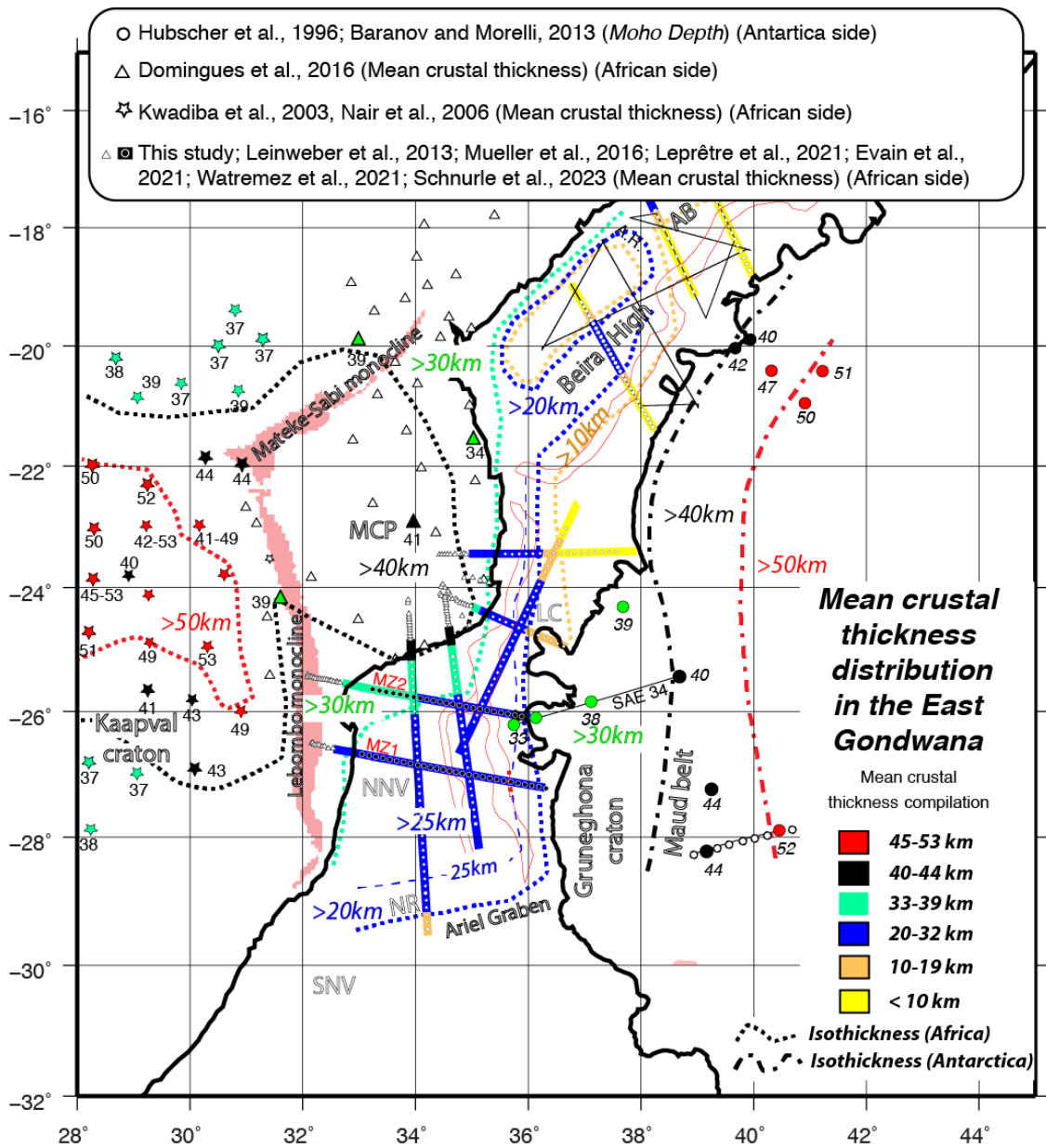


Figure 17

Figure 17 : Zooming on the tightest kinematic reconstruction of Thompson et al. (2019), with a compilation of a mean crustal thickness distribution in the East Gondwana, using published wide-angle results in Africa (Kwadiba et al., 2003, Nair et al., 2006; Leinweber et al., 2013; Domingues et al., 2016; Mueller et al., 2016) and in the Antarctica (Hubscher et al., 1996, modified from Kudryavtzev et al., 1991; Baranov and Morelli, 2013) together with the Pamela-MOZ3-5 wide-angle results (Moulin et al., 2020; Leprêtre et al., 2021; Evain et al., 2021; Watremez et al., 2021; Schnurle et al., 2023; this study). AB, Angoche Basin; AG, Ariel Graben; MCP, Mozambique Coastal Plain; NNV, North Natal Valley; NR, Naude Ridge; SNV, South Natal Valley; LC, Limpopo Corridor.

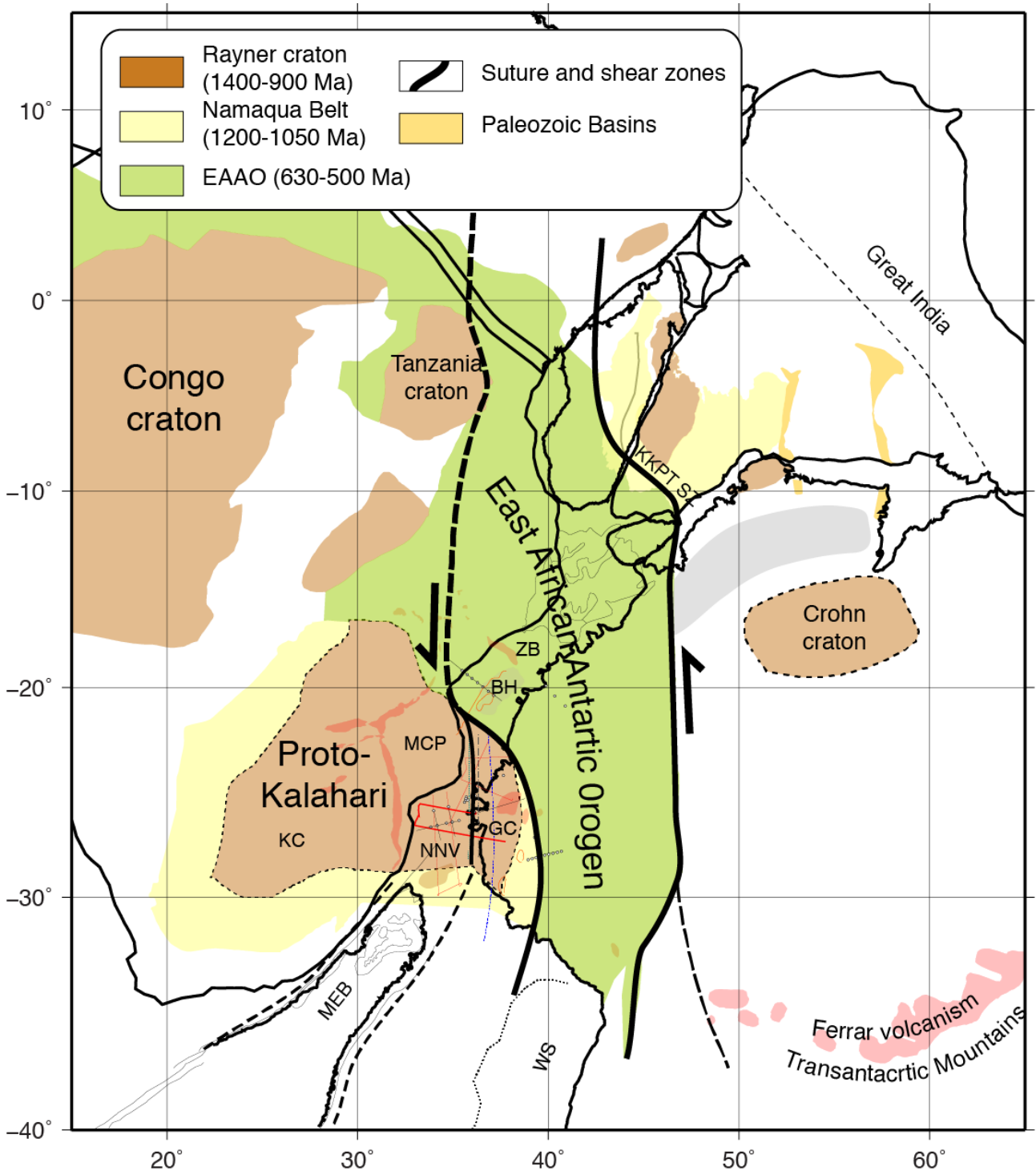


Figure 18